



Spanwise wall forcing can reduce turbulent heat transfer more than drag

Amirreza Rouhi¹ , Marcus Hultmark² and Alexander J. Smits² 

¹Department of Engineering, School of Science and Technology, Nottingham, Trent University, Nottingham NG11 8NS, UK

²Department of Mechanical and Aerospace Engineering, Princeton University, Princeton, NJ 08544, USA

Corresponding author: Amirreza Rouhi, amirreza.rouhi@ntu.ac.uk

(Received 14 June 2024; revised 15 January 2025; accepted 12 March 2025)

Direct numerical simulations are performed for turbulent forced convection in a half-channel flow with a wall oscillating either as a spanwise plane oscillation or to generate a streamwise travelling wave. The friction Reynolds number is fixed at $Re_{\tau_0} = 590$, but the Prandtl number Pr is varied from 0.71 to 20. For $Pr > 1$, the heat transfer is reduced by more than the drag, 40 % compared with 30 % at $Pr = 7.5$. This outcome is related to the different responses of the velocity and thermal fields to the Stokes layer. It is shown that the Stokes layer near the wall attenuates the large-scale energy of the turbulent heat flux and the turbulent shear stress, but amplifies their small-scale energy. At higher Prandtl numbers, the thinning of the conductive sublayer means that the energetic scales of the turbulent heat flux move closer to the wall, where they are exposed to a stronger Stokes layer production, increasing the contribution of the small-scale energy amplification. A predictive model is derived for the Reynolds and Prandtl number dependence of the heat-transfer reduction based on the scaling of the thermal statistics. The model agrees well with the computations for Prandtl numbers up to 20.

Key words: turbulence control, turbulence simulation, turbulent convection

1. Introduction

In many industrial applications, controlling heat transfer is as important as controlling drag. Some examples of the kinds of methods to control both drag and heat transfer are given in [figure 1](#). The performance of any given method is commonly based on the changes achieved in the skin-friction coefficient C_f and the Stanton number C_h , where

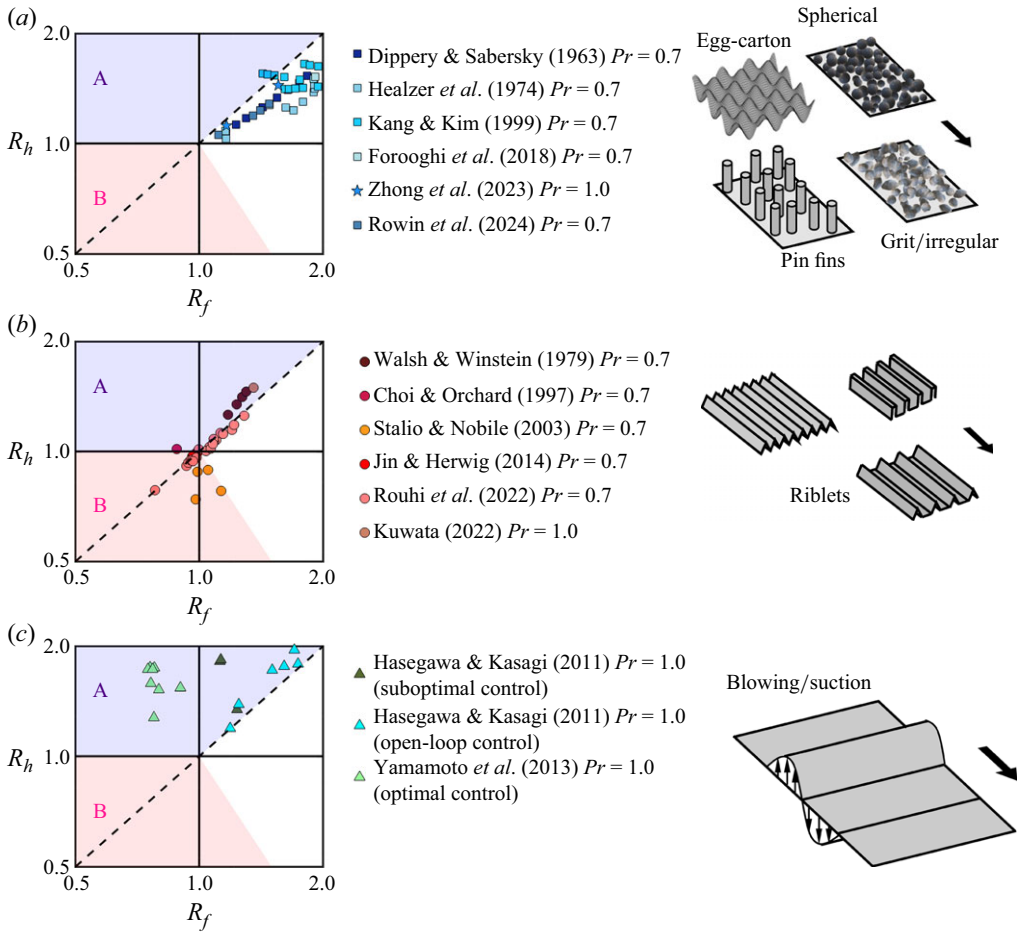


Figure 1. Performance plots showing the fractional changes in the skin-friction coefficient $R_f = C_f/C_{f_0}$ and Stanton number $R_h = C_h/C_{h_0}$ (log-log scale). The diagonal dashed line represents $R_h = R_f$. (a) Grit or irregular roughness (Dippery & Sabersky 1963; Forooghi *et al.* 2018), spherical roughness (Healzer *et al.* 1974), pin fins (Kang & Kim 1999) and egg-carton roughness (Zhong *et al.* 2023; Rowin *et al.* 2024). (b) Riblets (Walsh & Weinstein 1979; Choi & Orchard 1997; Stalio & Nobile 2003; Jin & Herwig 2014; Rouhi *et al.* 2022; Kuwata 2022). (c) Wall blowing/suction (Hasegawa & Kasagi 2011; Yamamoto *et al.* 2013). All data points are at $Pr = 0.7-1.0$.

$$C_f \equiv \frac{2\overline{\tau_w}}{\rho U_{ref}^2}, \quad C_h \equiv \frac{\overline{q_w}}{\rho c_p U_{ref} (T_w - T_{ref})}. \quad (1.1)$$

Here $\overline{\tau_w}$, $\overline{q_w}$, ρ , c_p and T_w are the wall shear stress, wall heat flux, fluid density, its specific heat capacity and wall temperature, respectively. The overbar in $\overline{\tau_w}$ and $\overline{q_w}$ represents averaging over the homogeneous directions and time. In a boundary layer, U_{ref} and T_{ref} are the free-stream velocity and temperature (Walsh & Weinstein 1979), and in a channel flow, U_{ref} and T_{ref} are the bulk velocity and either the bulk temperature (Stalio & Nobile 2003) or the mixed-mean temperature (Dippery & Sabersky 1963; MacDonald *et al.* 2019; Rouhi *et al.* 2022).

Figure 1 also shows the type of performance plot that is often used to measure the efficacy of control methods (Fan *et al.* 2009; Bunker 2013; Huang *et al.* 2017;

Rouhi *et al.* 2022). Here C_f and C_h are measured in the flow with control (the target case), and C_{f_0} and C_{h_0} are measured in the absence of control (the reference case), at matched Reynolds and Prandtl numbers. Some boundary layer studies match Reynolds numbers based on the free-stream velocity and the distance from the inlet (Walsh & Weinstein 1979; Choi & Orchard 1997). Some channel flow studies match Reynolds numbers based on the channel height and the bulk velocity (Stalio & Nobile 2003; Jin & Herwig 2014; Rouhi *et al.* 2022) or the friction velocity (MacDonald *et al.* 2019; Zhong *et al.* 2023). The diagonal dashed line represents equal fractional change in drag $R_f (= C_f/C_{f_0})$ and fractional change in heat transfer $R_h (= C_h/C_{h_0})$. In type A applications (shaded in purple), the objective is to maximise the heat transfer between the fluid and the solid surface, while minimising the drag. Examples include air passages in the gas turbine blades (Baek *et al.* 2022; Otto *et al.* 2022) or solar air collectors (Vengadesan & Senthil 2020; Rani & Tripathy 2022). In both applications, the air needs to absorb heat from the surface (turbine blade or absorber tube of the collector), yet the friction loss needs to be minimised through the passages. In type B applications (shaded in pink), the objective is to simultaneously minimise the heat transfer and drag between the fluid and the solid surface. Examples include transportation of crude oil (Yu *et al.* 2010; Han *et al.* 2015; Yuan *et al.* 2023) or transportation of industrial waste heat (Hasegawa *et al.* 1998; Ma *et al.* 2009; Xie & Jiang 2017). In these applications, a heated fluid is transported through pipelines to a long-distance demand site, and requires heat loss and friction loss to be minimised.

From figure 1(a) we see that rough surfaces and pin fins augment the heat transfer ($R_h > 1$), but for most data points, the drag increase exceeds the heat transfer increase ($R_f > R_h > 1$), and so they fall outside the objective space for either type A or B applications. Several phenomena contribute to the imbalance between R_f and R_h . The flow recirculations behind the roughness elements trigger pressure drag in C_f , in addition to the viscous drag. However, C_h consists of the wall heat flux only (MacDonald *et al.* 2019), which is the thermal analogue of the viscous stress. Additionally, the recirculation zones break the analogy between the viscous stress and the wall heat flux (MacDonald *et al.* 2019), and the analogy between the turbulent shear stress and the turbulent heat flux (Kuwata 2021). Also, by increasing the roughness size, the conductive sublayer becomes thinner than the viscous sublayer (MacDonald *et al.* 2019; Zhong *et al.* 2023).

In figure 1(b) we show the performance of riblets, as two-dimensional streamwise-aligned surface protrusions that do not induce pressure drag. Most data points are scattered near $R_h = R_f$, but a few data points fall into the regions of interest for type A or B applications. Rouhi *et al.* (2022) and Kuwata (2022) relate such behaviour to the formation of Kelvin–Helmholtz rollers and secondary flows by certain riblet designs.

Figure 1(c) shows the data points for wall blowing/suction in a turbulent channel flow. All data points fall into the objective space for type A applications. The data points that noticeably yield $R_h > R_f$ are from the application of a suboptimal control framework (Lee *et al.* 1998) or an optimal control framework (Bewley *et al.* 2001). Especially, the optimal control application results in simultaneous heat-transfer augmentation and drag reduction ($R_h > 1 > R_f$). Hasegawa & Kasagi (2011) and Yamamoto *et al.* (2013) discovered that both the optimal and suboptimal control inputs exhibit characteristics similar to a travelling wave. When the coherent part of the suboptimal control inputs are applied as an open-loop control framework, the data points fall closer to $R_h = R_f$.

In the present study we focus on wall oscillation either as a spanwise oscillating plane or a streamwise travelling wave, as described by

$$W_s(x, t) = A \sin(\kappa_x x + \omega t), \quad (1.2)$$

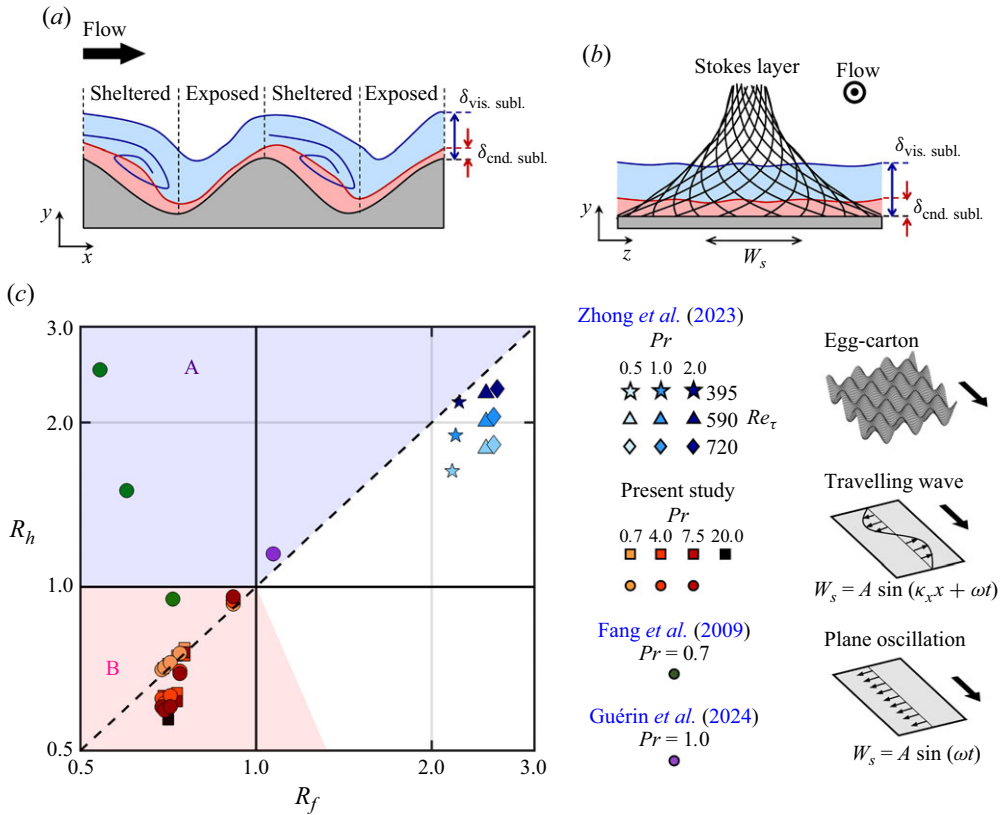


Figure 2. Effect of Pr on the performance of egg-carton roughness by Zhong *et al.* (2023), plane oscillation and a travelling wave from the present study (table 1), and plane oscillation by Fang *et al.* (2009) and Guérin *et al.* (2024). Star, triangle and diamond symbols represent egg-carton roughness, square symbols represent a streamwise travelling wave ($\kappa_x \neq 0$ in (1.2)), and circle symbols represent plane oscillation ($\kappa_x = 0$ in (1.2)). Panels (a,b) illustrate the different physics underlying the wall heat transfer over roughness and wall oscillation for $Pr > 1$; $\delta_{vis. subl.}$ and $\delta_{cnd. subl.}$ respectively indicate the viscous sublayer and conductive sublayer thicknesses. Panel (c) compiles all the data points in the performance plot.

where W_s is the instantaneous spanwise surface velocity that oscillates with amplitude A and frequency ω . With $\kappa_x \neq 0$, the mechanism generates a streamwise travelling wave, and with $\kappa_x = 0$ the motion is a simple spanwise oscillating plane (as illustrated in figure 2). We denote the former case as a travelling wave, and the latter one as plane oscillation. The drag performance of (1.2) has been extensively investigated in the literature (Jung *et al.* 1992; Quadrio & Sibilla 2000; Quadrio *et al.* 2009; Viotti *et al.* 2009; Quadrio & Ricco 2011; Quadrio 2011; Gatti & Quadrio 2013; Hurst *et al.* 2014; Gatti & Quadrio 2016; Marusic *et al.* 2021; Rouhi *et al.* 2023; Chandran *et al.* 2023).

Dimensional analysis for the drag yields

$$R_f = \frac{C_f}{C_{f_0}} = f_f(A^+, \kappa_x^+, \omega^+, Re_{\tau_0}) \quad (1.3)$$

(Marusic *et al.* 2021; Rouhi *et al.* 2023). The superscript ‘+’ indicates normalisation using the viscous velocity ($u_{\tau_0} = \sqrt{\tau_{w_0}/\rho}$) and length (ν/u_{τ_0}) scales, where ν is the fluid kinematic viscosity. The superscript ‘*’ indicates viscous scaling based on the actual friction velocity, that is, u_{τ} of the drag-altered flow for the actuated cases. For the heat

Non-actuated		Travelling wave $A^+ = 12, \kappa_x^+ = 0.0014$			Oscillating plane $A^+ = 12$		
$L_x, L_z = 2.7h, 0.85h$ $\Delta_x^+, \Delta_z^+ = 8.3, 3.9$ $\Delta_y^+ = 0.28 - 8.5$		$L_x, L_z = 7.6h, 0.85h$ $\Delta_x^+, \Delta_z^+ = 8.8, 3.9$ $\Delta_y^+ = 0.28 - 8.5$			$L_x, L_z = 2.7h, 0.85h$ $\Delta_x^+, \Delta_z^+ = 8.3, 3.9$ $\Delta_y^+ = 0.28 - 8.5$		
$C_{f_0} \times 10^{-3}$	$C_{h_0} \times 10^{-4}$	ω^+	DR %	HR %	ω^+	DR %	HR %
5.71	33.82	0.022	25.2	23.6	0.022	8.6	7.3
		0.044	30.6	29.3	0.044	25.9	24.7
		0.066	30.5	29.1	0.066	31.1	29.6
		0.088	29.3	27.9	0.088	30.3	28.9
		0.110	26.8	25.3	0.110	28.7	27.4
$Pr = 0.71$							
5.71	14.14	0.022	24.5	25.3	0.022	9.5	5.9
		0.044	31.0	37.0	0.044	25.9	30.1
		0.066	30.7	38.4	0.066	30.4	37.8
		0.088	29.1	37.3	0.088	30.6	39.0
		0.110	27.6	36.2	0.110	28.2	36.9
$Pr = 4.0$							
5.72	9.90	0.022	25.6	24.0	0.022	9.7	4.3
		0.044	31.8	37.7	0.044	26.5	30.8
		0.066	30.7	39.8	0.066	31.3	40.0
		0.088	30.5	40.4	0.088	30.2	40.7
		0.110	27.5	38.0	0.110	28.7	39.8
$Pr = 7.5$							
5.71	5.47	0.088	29.5	43.5	$Pr = 20.0$		

Table 1. Production calculations at $Re_{\tau_0} = 590$ (reduced domain $L_x \geq 2.7h, L_z = 0.85h$). Non-actuated cases (left column, figure 3a). Travelling wave cases (middle column, figure 3b). Spanwise plane oscillation cases (right column, figure 3c). Each row represents one simulation case. The domain and grid sizes for each configuration are reported at the top.

transfer, we need to include the Prandtl number $Pr = \nu/\alpha$, where α is the fluid thermal diffusivity, and we find that

$$R_h = \frac{C_h}{C_{h_0}} = f_h(A^+, \kappa_x^+, \omega^+, Re_{\tau_0}, Pr). \tag{1.4}$$

The drag reduction (DR) is given by $DR = 1 - R_f$, and the heat-transfer reduction (HR) is given by $HR = 1 - R_h$. For HR, we have a five-dimensional parameter space (1.4) that is investigated over a limited extent (Fang *et al.* 2009, 2010; Guérin *et al.* 2024), as shown in figure 2. These studies consider spanwise plane oscillation ($\kappa_x^+ = 0$) in a turbulent channel flow at $Re_{\tau_0} = hu_{\tau_0}/\nu \simeq 180$ and $Pr \simeq 0.7 - 1.0$. Fang *et al.* (2009, 2010) consider three cases with $T_{osc}^+ = 2\pi/\omega^+ = 100$ and $A^+ = 6, 13, 19$, and Guérin *et al.* (2024) consider one case with $T_{osc}^+ = 500$ and $A^+ = 30$. These cases fall into the objective space for type A applications (except one case with $R_f < 1, R_h \simeq 1$).

Figure 2 highlights that we are at an early stage in terms of our knowledge of HR for the surface actuation (1.2), and just like the investigations on DR, we need to explore different parameters of (1.4) as a build up process. Comparing (1.4) with (1.3), Pr is a key parameter that differentiates R_h from R_f , and it leads to their significant disparity (figure 2). Furthermore, the fluids for type B applications have $Pr \gg 1$ (e.g. crude oil). Therefore, in the present study we focus on Pr and ω^+ as our parameters of interest (figure 2 and table 1). We conduct direct numerical simulations (DNS) of turbulent forced

convection in a half-channel flow with fix $A^+ = 12$ and $Re_{\tau_0} = 590$, and we consider two values for κ_x^+ to simulate plane oscillation ($\kappa_x^+ = 0$) and a travelling wave ($\kappa_x^+ = 0.0014$, $\lambda^+ = 2\pi/\kappa_x^+ \simeq 4500$). We consider $Pr = 0.71$ (air), 4.0, 7.5 (water) and 20 (molten salt). At each $0.71 \leq Pr \leq 7.5$, we systematically vary ω^+ from 0.022 to 0.110, corresponding to the regime where we expect DR to reach 30 % (Gatti & Quadrio 2016; Rouhi *et al.* 2023). Our preference for the present actuation parameters is motivated by an existing surface-actuation test bed (Marusic *et al.* 2021; Chandran *et al.* 2023) that can operate under these conditions. This provides the opportunity to extend the present numerical study through experiment. As the first study that investigates Pr effects for this problem, we conduct a thorough study of grid resolution requirements for our considered parameter space (Appendix A).

As an overview, we note that all our results give a decrease in drag and heat transfer, with maximum DR = 30 % and HR = 40 % (see figure 2). For Prandtl numbers greater than one, however, HR increases more than DR. The results fall into the objective space for type B applications, a space that has largely been neglected in the past despite its industrial relevance. The surfaces that we reviewed in figure 1 consider $Pr = 0.7 - 1.0$, however, we anticipate that their performances will change with increasing Pr . For instance, in figure 2 we overlay the data points of egg-carton roughness at $Pr = 0.5, 1.0, 2.0$ by Zhong *et al.* (2023). Unlike plane oscillation or a travelling wave, the roughness data points approach $R_h = R_f$ with increasing Pr because heat transfer over these two surface types is governed by different flow mechanisms that are unique to each surface, leading to different trends with Pr . Over the rough surface (figure 2a), variation of C_h with Pr depends on the area fraction of the sheltered and exposed regions, associated with the recirculation and attached zones that follow different local Pr scalings (Zhong *et al.* 2023; Rowin *et al.* 2024). Over the surface oscillation (figure 2b), the variation of C_h with Pr is an aspect that we investigate in the present study. We discover that by increasing Pr and thinning of the conductive sublayer, the Stokes layer, formed in response to the wall oscillation, transfers more energy to the near-wall temperature scales than the velocity scales. We also find that HR yields different Pr scaling depending on the actuation parameters. In § 3.5 we derive a model that predicts that plane oscillation and a travelling wave can reduce the heat loss beyond 50 % for $Pr \gtrsim \mathcal{O}(10^2)$, a regime that is important for crude oil transportation through pipelines. Our model is supported by our DNS data point at $Pr = 20$ that yields HR = 43 % (black square in figure 2).

2. Numerical flow set-up

2.1. Governing equations and simulation set-up

The governing equations for an incompressible fluid with constant ρ , ν and thermal diffusivity α are solved in a half-channel flow (figure 3), where

$$\nabla \cdot \mathbf{U} = 0, \tag{2.1}$$

$$\frac{\partial \mathbf{U}}{\partial t} + \nabla \cdot (\mathbf{U}\mathbf{U}) = -\frac{1}{\rho} \nabla p + \nu \nabla^2 \mathbf{U} - \frac{1}{\rho} \frac{d\bar{P}}{dx} \hat{\mathbf{e}}_x, \tag{2.2}$$

$$\frac{\partial \Theta}{\partial t} + \nabla \cdot (\mathbf{U}\Theta) = \alpha \nabla^2 \Theta - U \frac{dT_w}{dx}, \tag{2.3}$$

and (2.1), (2.2) and (2.3) are the continuity, velocity and temperature transport equations, respectively. We ignore buoyancy, as appropriate for forced convection. In our notation, $\mathbf{U} = (U, V, W)$ is the velocity vector, and x, y and z are the streamwise, wall-normal and spanwise directions, respectively. In (2.2) the total pressure gradient was decomposed into

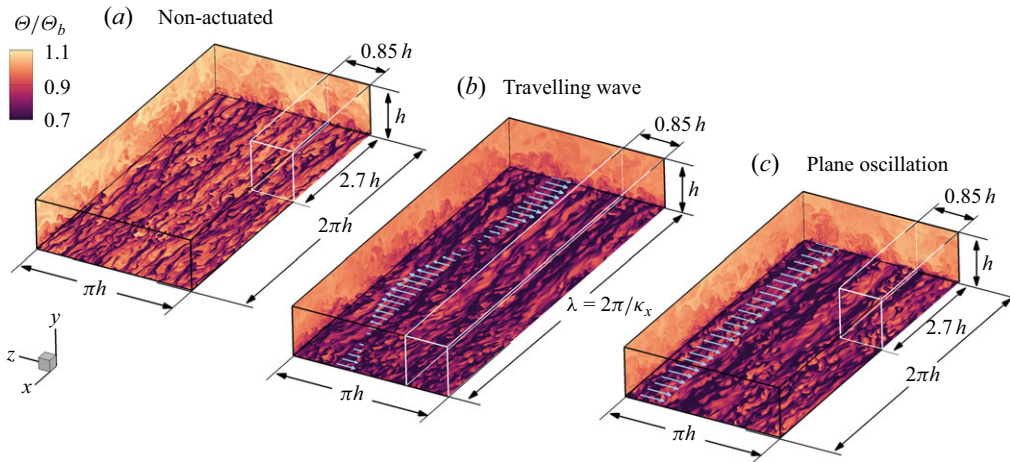


Figure 3. Computational configurations in a half-channel flow for the present study. (a) Non-actuated case as the reference. (b) Actuated case with the travelling wave with $A^+ = 12$, $\kappa_x^+ = 0.0014$; the domain length encompasses one wavelength $L_x = 2\pi/\kappa_x \simeq 7.6h$. (c) Actuated case with spanwise plane oscillation with $A^+ = 12$. In (b,c) we overlay the instantaneous wall motion as a vector field. Full domain shown by the large box with black edges; reduced domain shown by the small box with white edges. In (a,b,c) we visualise the instantaneous fields of Θ at $y^+ = 15$, $Re_{\tau_0} = 590$ and $Pr = 7.5$, and for $\omega^+ = 0.088$ in (b,c).

the driving (mean) part $d\bar{P}/dx$ and the periodic part ∇p . Similarly, the total temperature $T = (dT_w/dx)x + \Theta$ was decomposed into the mean part dT_w/dx and the periodic part Θ . This thermal driving approach imposes a prescribed mean heat flux at the wall, making it a suitable boundary condition for a periodic domain, and it has been widely used for the simulation of forced convection in a channel flow (Kasagi *et al.* 1992; Watanabe & Takahashi 2002; Stalio & Nobile 2003; Jin & Herwig 2014; Alcántara-Ávila & Hoyas 2021; Alcántara-Ávila *et al.* 2021; Rouhi *et al.* 2022). By averaging (2.2) and (2.3) in time and over the entire fluid domain, we obtain

$$-\frac{1}{\rho} \frac{d\bar{P}}{dx} h = \frac{\bar{\tau}_w}{\rho} \equiv u_\tau^2, \quad -U_b \frac{dT_w}{dx} h = \frac{\bar{q}_w}{\rho c_p} \equiv \theta_\tau u_\tau, \quad (2.4a,b)$$

where $\bar{\tau}_w$ and \bar{q}_w are respectively the xz plane and time-averaged wall shear stress and wall heat flux, U_b is the bulk velocity, h is the half-channel height, u_τ and θ_τ are the friction velocity and friction temperature, and c_p is the specific heat capacity. We adjust $d\bar{P}/dx$ based on a target flow rate (namely, a bulk Reynolds number $Re_b \equiv U_b h/\nu$) that is matched between the non-actuated reference case (figure 3a) and the actuated cases (figure 3b,c).

Equations (2.1)–(2.3) are solved using a fully conservative fourth-order finite difference code, employed by previous DNS studies of thermal convection (Ng *et al.* 2015; Rouhi *et al.* 2021; Zhong *et al.* 2023; Rowin *et al.* 2024). The half-channel flow has periodic boundary conditions in the streamwise and spanwise directions (figure 3). The bottom-wall velocity boundary conditions are $U = V = W = 0$ for the non-actuated case (figure 3a), $U = V = 0$, $W = A \sin(\kappa_x x + \omega t)$ for the actuated case with the travelling wave (figure 3b) and $U = V = 0$, $W = A \sin(\omega t)$ for the actuated case with the spanwise plane oscillation (figure 3c). The top boundary conditions for the velocity are the free-slip and impermeable conditions ($\partial U/\partial y = \partial W/\partial y = V = 0$). The boundary conditions for Θ at the bottom wall and top boundary are $\Theta = 0$ and $\partial \Theta/\partial y = 0$, respectively. In other words, the total temperature at the bottom wall increases linearly in the x direction $T = (dT_w/dx)x$,

and at the top boundary the boundary condition is adiabatic ($\partial T/\partial y = 0$). Past studies have employed half-channel flow to study turbulent flow over complex surfaces (Yuan & Piomelli 2014; MacDonald *et al.* 2017; Rouhi *et al.* 2019). This configuration has a lower computational cost compared with the conventional Poiseuille channel flow with a no-slip condition at the bottom and top walls. Yet the two configurations have almost identical mean velocity profiles up to the logarithmic region, and similar turbulent stresses (Yao *et al.* 2022). This is also supported in Appendix A, where we obtain very similar mean velocity and turbulent stress profiles between our non-actuated half-channel flow and the DNS of a Poiseuille channel flow by Moser *et al.* (1999) (figure 25*a,b*), and the values of C_{f_0} differ by less than 2%.

Throughout this paper, we call Θ the temperature. We denote the xz plane and time-averaged quantities with overbars (e.g. $\overline{\Theta}$ is the plane and time averaged Θ) and the turbulent quantities with lowercase letters (e.g. θ is the turbulent temperature). Following this notation, $\overline{u^2}$ and \overline{uv} are the turbulent stress components, and $\overline{\theta^2}$ and $\overline{\theta v}$ are their analogue for the turbulent temperature fluxes.

2.2. Simulation cases

Table 1 summarises the production calculations. All the calculations were performed at a fixed bulk Reynolds number $Re_b \simeq 11004$, equivalent to a friction Reynolds number $Re_{\tau_0} = 590$ for the non-actuated flow. The grid sizes are $\Delta_x^+ \times \Delta_z^+ \simeq 8 \times 4$, $\Delta_y^+ = 0.28 - 8.5$, chosen based on extensive validation studies (Appendix A). In comparison, Alcántara-Ávila & Hoyas (2021) used $\Delta_x^+ \times \Delta_z^+ \simeq 8 \times 4$, $\Delta_y^+ = 0.27 - 5.3$ for the turbulent channel flow at $Re_{\tau_0} = 500$ and $1 \leq Pr \leq 7$, and Pirozzoli (2023) used $\Delta_x^+ \times \Delta_z^+ \simeq 10 \times 4.5$ with 30 points within $y^+ \leq 40$ for the turbulent pipe flow at $Re_{\tau_0} \simeq 1100$ and $Pr \leq 16$. Here, we have 60 points within $y^+ \leq 40$. As shown in Appendix A, we obtain less than 2% difference in DR and HR when using finer resolutions than our production calculation grids, and find very good agreement in the first- and second-order velocity and temperature statistics as well as their spectrograms (figures 25 to 27).

To reduce the computational cost, the production calculations were performed in a reduced domain rather than a full-domain conventional channel flow (see figure 3). Because of the domain truncation, the flow is fully resolved up to a fraction of the domain height $y_{res} < h$ (figure 4). In the past, the reduced-domain channel flow has been used for accurate calculation of the drag and the near-wall turbulence over various static and deforming surfaces, including egg-carton roughness with $y_{res}^+ \lesssim 250$ (MacDonald *et al.* 2017, 2018), riblets with $y_{res}^+ \simeq 100$ (Endrikat *et al.* 2021) and travelling waves with $y_{res}^+ \lesssim 1000$ (Gatti & Quadrio 2016; Rouhi *et al.* 2023). The reduced-domain channel flow has also been employed for accurate calculation of the wall heat flux and the near-wall thermal field over rough surfaces with $y_{res}^+ \lesssim 600$ (MacDonald *et al.* 2019; Zhong *et al.* 2023; Rowin *et al.* 2024), and riblets with $y_{res}^+ \simeq 100$ (Rouhi *et al.* 2022). In our case, as shown in Appendix A, with $\Delta_x^+ \times \Delta_z^+ \simeq 8 \times 4$ the difference between the reduced and full domains is less than 1% in terms of DR and HR. Furthermore, the results for the two domain sizes agree well in terms of the statistics of velocity and temperature, and their spectrograms (figures 26 and 27). For the reduced-domain sizes, we follow the prescriptions by Chung *et al.* (2015) and MacDonald *et al.* (2017), which were extended to the travelling wave actuation case by Rouhi *et al.* (2023). The resolved height y_{res}^+ needs to fall in the logarithmic region, and the domain width L_x^+ and length L_z^+ are adjusted so that $L_z^+ \simeq 2.5y_{res}^+$ and $L_x^+ \gtrsim \max(3L_z^+, 1000, \lambda^+)$, where $\lambda = 2\pi/\kappa_x$ is the travelling wavelength. Here, we chose $y_{res}^+ = 200$, which resolves up to a third of the half-channel height. Hence, the domain sizes are $L_x \times L_z \simeq 2.7h \times 0.85h$ for the non-actuated and

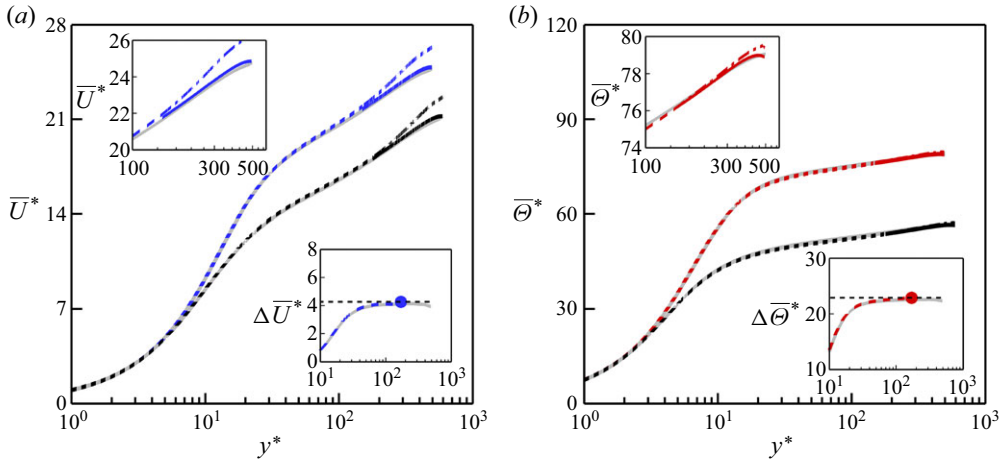


Figure 4. Comparison at $Re_{\tau_0} = 590$ of (a) mean velocity \bar{U}^* and (b) mean temperature $\bar{\Theta}^*$ between the full-domain (grey lines) and reduced-domain half-channel flow (black, blue and red lines). Black lines: non-actuated case at $Pr = 7.5$. Blue and red lines: travelling wave case at $Pr = 7.5$ with $A^+ = 12$, $\kappa_x^+ = 0.0014$, $\omega^+ = 0.088$. For the reduced-domain cases, the resolved portion is shown with a dashed line ($y^* \lesssim 170$) and the unresolved portion is shown with a dashed-dotted line ($y^* \gtrsim 170$). The unresolved portion is replaced by the reconstructed profiles (solid lines), as explained in § 2.3. The insets plot the velocity and temperature differences $\Delta \bar{U}^*$ and $\Delta \bar{\Theta}^*$; bullets mark $y_{res}^* = 170$, where we obtain the log-law shifts $\Delta \bar{U}_{log}^*$ and $\Delta \bar{\Theta}_{log}^*$.

plane oscillation cases (figure 3a,c). For the travelling wave cases, however, L_x cannot be truncated because it is constrained by the travelling wavelength $\lambda \simeq 7.6h$, and so we use $L_x \times L_z \simeq 7.6h \times 0.85h$ (figure 3b). For the actuated cases, y_{res} scaled by the actuated (drag-reduced) friction velocity is $170 \lesssim y_{res}^* \lesssim 190$ (that is, less than 200). Therefore, $y_{res}^* = 170$ is taken to be the maximum resolved height for all our cases.

2.3. Calculating the skin-friction coefficient and Stanton number

We can write the skin-friction coefficient and Stanton number as $C_f = 2/U_b^{*2}$ and $C_h = 1/(U_b^* \Theta_b^*)$. Although some studies use the mixed-mean temperature to define C_h (MacDonald *et al.* 2019; Rouhi *et al.* 2022; Zhong *et al.* 2023), we use the bulk temperature Θ_b as adopted by Stalio & Nobile (2003) and Kuwata (2022), primarily because it is more straightforward to derive a predictive model for HR with this definition (Appendix B). For our cases, there is only a maximum 2% difference between C_h based on Θ_b and the one based on the mixed-mean temperature.

For the full-domain half-channel flow, the mean velocity \bar{U}^* and temperature $\bar{\Theta}^*$ are fully resolved across the entire domain (grey profiles in figure 4), and so U_b^* and Θ_b^* can be obtained by direct integration of \bar{U}^* and $\bar{\Theta}^*$. For the reduced-domain half-channel flow, we first need to construct \bar{U}^* and $\bar{\Theta}^*$ beyond y_{res}^* (Rouhi *et al.* 2022, 2023). In figure 4 we see that the resolved portions of the \bar{U}^* and $\bar{\Theta}^*$ profiles up to $y_{res}^* \simeq 170$ are in excellent agreement with the full-domain profiles. Beyond y_{res}^* , however, the flow is unresolved due to the domain truncation, appearing as a fictitious wake in the \bar{U}^* and $\bar{\Theta}^*$ profiles (dashed-dotted lines in figure 4). The fictitious wake is weaker for the $\bar{\Theta}^*$ profile at $Pr = 7.5$ than the \bar{U}^* profile, which could also be regarded as a $\bar{\Theta}^*$ profile at $Pr = 1.0$. In other words, the domain truncation affects $\bar{\Theta}^*$ to a lesser degree by increasing Pr . Nevertheless, even for the \bar{U}^* profile, the fictitious wake is constrained to $y^* \gtrsim 170$. We replace these

unresolved portions with the composite profiles of \bar{U}^* and $\bar{\Theta}^*$ (see (C1a), (C1b) in Appendix B). For this, we need the log-law shifts $\Delta\bar{U}_{log}^*$ and $\Delta\bar{\Theta}_{log}^*$ in (C1a) and (C1b), which we obtain by plotting $\Delta\bar{U}^* = \bar{U}^* - \bar{U}_0^*$ and $\Delta\bar{\Theta}^* = \bar{\Theta}^* - \bar{\Theta}_0^*$, the differences between the actuated and non-actuated cases (see figure 4). Finally, we find U_b^* and Θ_b^* by integrating the resolved portion of the profiles up to y_{res}^* and the reconstructed portion beyond y_{res}^* . By applying this profile reconstruction, we obtain less than 1 % difference in C_f and C_h between the full-domain case and the reduced-domain case (Appendix A).

3. Results

3.1. Overall variations of DR and HR

The values of HR, DR and the difference HR – DR are shown in figure 5. For all cases considered, HR and DR initially increase with the frequency of forcing, but for $\omega^+ \gtrsim 0.04$, they reach a maximum value before slowly decreasing at higher frequencies. The maximum DR is approximately 30 % for all Prandtl numbers, but the maximum HR increases from 30 % to approximately 40 % with increasing Prandtl number, marking a significant disparity between DR and HR. The increasing disparity towards HR > DR occurs for $\omega^+ \geq 0.04$, however, at $\omega^+ = 0.022$, HR \lesssim DR. The comparison between the reduced-domain results (filled squares) and the full-domain results (open circles) supports the reliability of the production runs. At $Pr = 7.5$, the reduced-domain grid is more than twice as coarse as the full-domain grid, yet there is less than 2 % difference in DR and HR (Appendix A gives more details). The trends in DR seen here have been widely recorded in the previous literature, as the review by Ricco *et al.* (2021) makes clear. However, to the best of the authors’ knowledge, the behaviour of HR has not been reported before. In § 3.4 we relate the observed trends between HR and DR to the attenuation in the turbulent shear stress $\bar{u}\bar{v}$ and turbulent scalar flux $\bar{\theta}v$, followed by studying their interactions with the Stokes layer (§ 3.6–3.8).

In figure 6 we plot the plane oscillation data of DR and HR at close $Pr = 0.71 - 1.0$ from our present study (figure 5b), Guérin *et al.* (2024) and Fang *et al.* (2009). Unlike our data, the two cited studies obtain heat transfer increase (HR \lesssim 0). Compared with Guérin *et al.* (2024), our A^+ values differ by 2.5 times and ω^+ values differ by 1.7 times. Nevertheless, based on our findings from §§ 3.6 to 3.8, we speculate that HR < DR < 0 by Guérin *et al.* (2024) is related to the highly protrusive Stokes layer (beyond 50 viscous units) for $\omega^+ < 0.04$ (figure 22). Compared with Fang *et al.* (2009), we have close values of A^+ and ω^+ . At $A^+ \simeq 12.0$ and $\omega^+ \simeq 0.06$, the DR values differ by 9 % between Fang *et al.* (2009) (DR = 40 %, $Re_{\tau_0} = 180$) and our study (DR = 31 % at $Re_{\tau_0} = 590$); this is due to the Reynolds number difference, as discussed in the literature (Gatti & Quadrio 2016; Marusic *et al.* 2021; Rouhi *et al.* 2023). However, the values of HR have opposite signs and are different by 80 %, HR = 30 % from our study versus HR = –50 % from Fang *et al.* (2009). In addition to Re_{τ_0} , we speculate that such a difference is related to the different computational set-ups. We conduct DNS of incompressible turbulent channel flow with $\Delta_x^+ \times \Delta_z^+ = 8.3 \times 3.9$, while Fang *et al.* (2009) conduct large-eddy simulation (LES) of compressible turbulent channel flow (Mach number $Ma = 0.5$) with $\Delta_x^+ \times \Delta_z^+ = 35 \times 12$.

3.2. Optimal actuation frequency

Figure 5 indicates that for the considered cases, the optimal actuation frequency for DR is $\omega^+ \approx 0.044$ for the travelling wave and ≈ 0.066 for the plane oscillation, regardless of the Prandtl number. For HR, the optimal frequency coincides with that for DR at $Pr = 0.71$, but it increases to 0.088 for both types of actuation as the Prandtl number increases to 7.5.

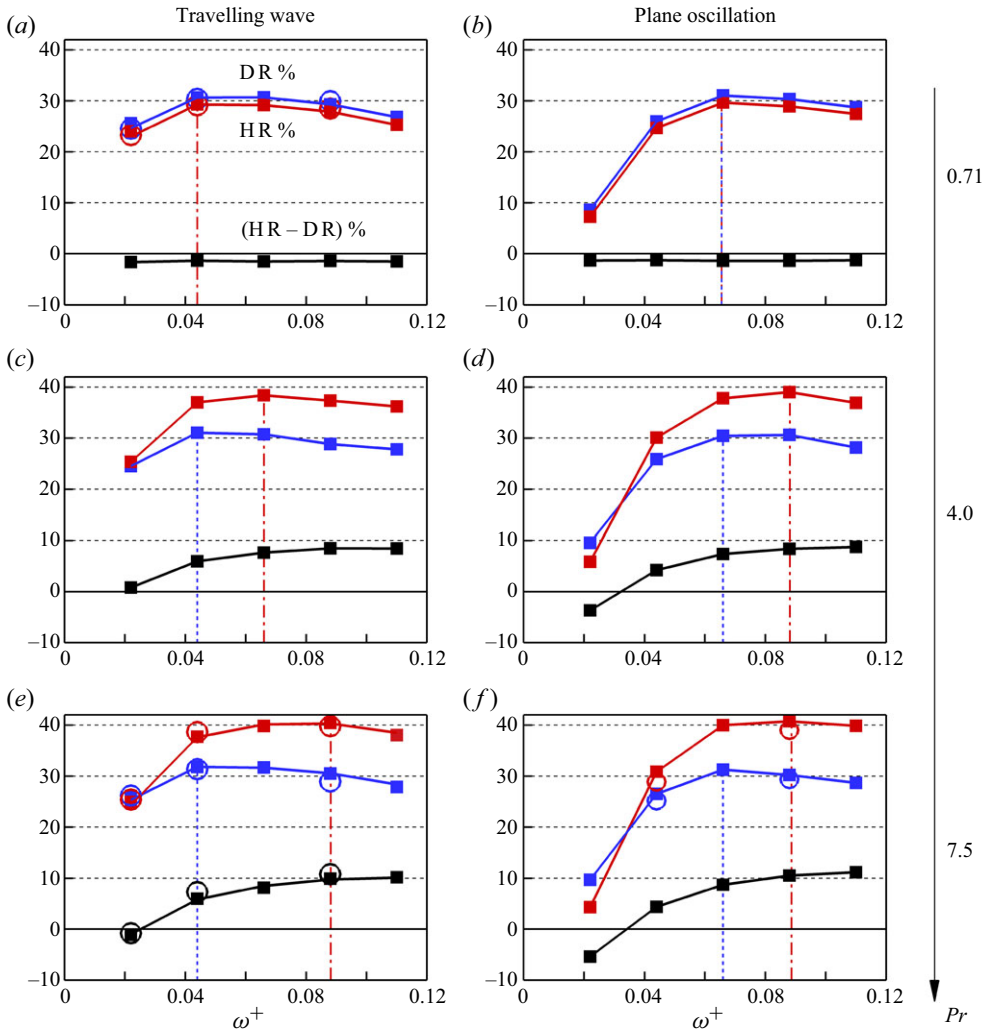


Figure 5. Values of DR % (blue symbols), HR % (red symbols) and their difference (black symbols) for the cases given in table 1. Filled squares: reduced-domain simulations; empty circles: full-domain simulations. Blue dashed line marks the maximum DR; red dashed-dotted line marks the maximum HR.

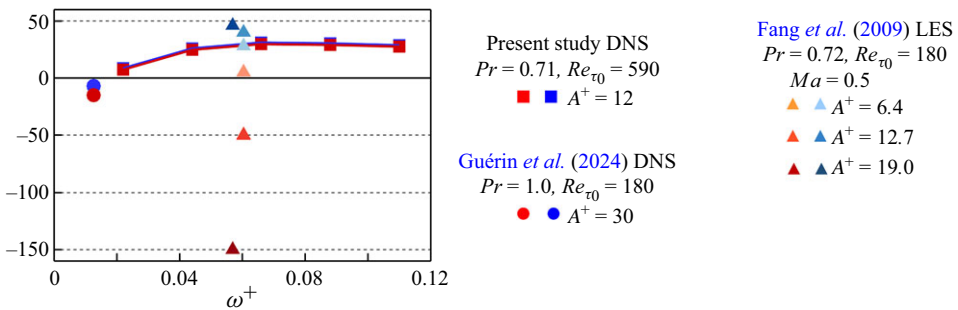


Figure 6. Plane oscillation data of DR % (blue symbols) and HR % (orange/red symbols) at $Pr = 0.7 - 1.0$ from our present study, Guérin et al. (2024), and Fang et al. (2009).

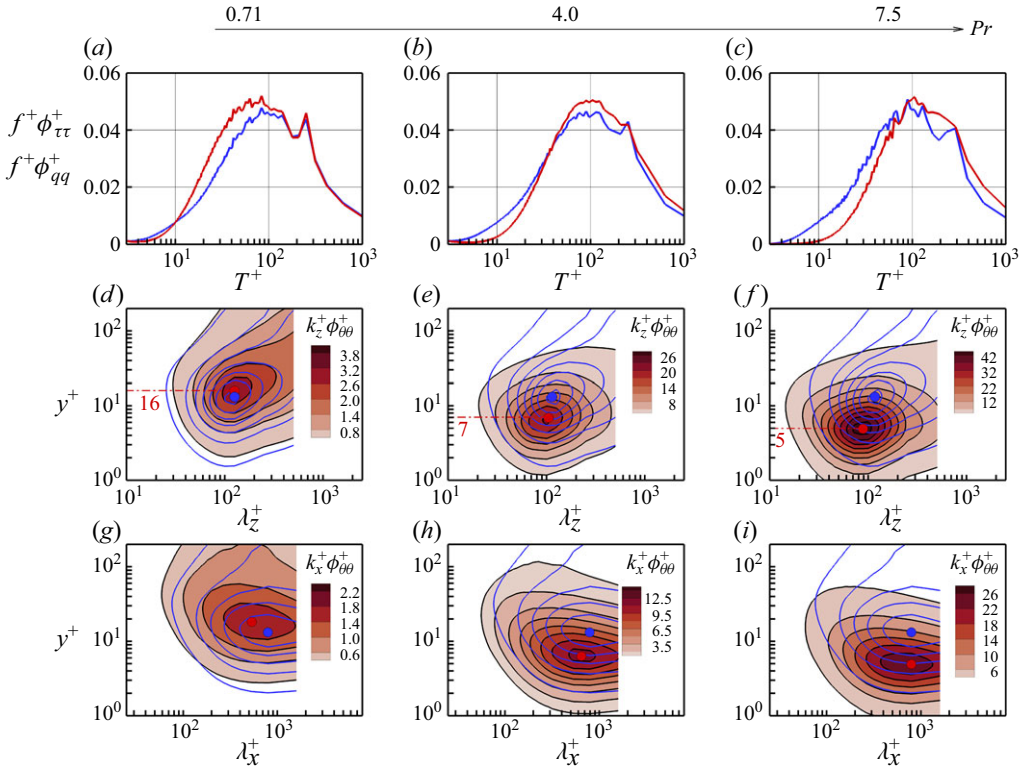


Figure 7. Non-actuated half-channel flow with increasing Prandtl number: (a,d,g) $Pr = 0.71$, (b,e,h) $Pr = 4.0$, (c,f,i) $Pr = 7.5$. (a–c) Pre-multiplied frequency spectra of wall shear stress $f^+ \phi_{\tau\tau}^+$ (blue line) and wall heat flux $f^+ \phi_{qq}^+$ (red line), where $T^+ = 1/f^+$. (d–f) Spectrograms of the streamwise velocity fluctuations (blue contour lines) and temperature fluctuations (filled contour) pre-multiplied by the spanwise wavenumber k_z^+ . (g–i) Same as (d–f), pre-multiplied by the streamwise wavenumber k_x^+ . Contour levels for $k_z^+ \phi_{uu}^+$ start from 0.2 to 3.8 with an increment of 0.6; contour levels for $k_x^+ \phi_{uu}^+$ start from 0.2 to 2.2 with an increment of 0.4. The blue and red bullets in (d–f) locate the maximum in $k_z^+ \phi_{uu}^+$ and $k_z^+ \phi_{\theta\theta}^+$, respectively, and in (g–i) locate the maximum in $k_x^+ \phi_{uu}^+$ and $k_x^+ \phi_{\theta\theta}^+$, respectively.

Previous studies relate the optimal frequency for DR to the characteristic time scale of the energetic velocity scales associated with the near-wall cycle of turbulence, \mathcal{T}_u^+ (Quadrio *et al.* 2009; Chandran *et al.* 2023). When the actuation period $T_{osc}^+ \equiv 2\pi/\omega^+$ matches this time scale, the wall oscillation becomes more effective in disrupting the near-wall scales, leading to the maximum DR (Ricco *et al.* 2021). Chandran *et al.* (2023) discuss this interaction using the pre-multiplied spectrum of wall shear stress $f^+ \phi_{\tau\tau}^+$, and the corresponding spectra for our non-actuated case are shown in figure 7(a–c) (blue lines). In agreement with Chandran *et al.* (2023), the peaks in the shear stress spectra occur at $\mathcal{T}_u^+ \simeq 100$, corresponding to $\omega^+ \simeq 0.063$, which broadly matches the frequencies of actuation for maximum DR found here.

Figure 7 also shows the corresponding spectra for the fluctuating wall heat flux, $f^+ \phi_{qq}^+$ (red lines), as well as the pre-multiplied spectrograms of the fluctuating streamwise velocity and temperature ($k_z^+ \phi_{uu}^+$, $k_x^+ \phi_{uu}^+$, $k_z^+ \phi_{\theta\theta}^+$, $k_x^+ \phi_{\theta\theta}^+$). Figure 7(a,b,c) reveals that while $f^+ \phi_{qq}^+$ is sensitive to Pr at small time scales ($T^+ \lesssim 70$), the time scale of the energetic temperature scales $\mathcal{T}_\theta^+ \simeq 100$ is insensitive to Pr , and coincides with \mathcal{T}_u^+ . The streamwise and spanwise lengths of the energetic temperature scales vary somewhat with

Prandtl number (see figure 7*d-i*), but they also remain close to the length scales of the energetic velocity scales. However, the peak in $k_z^+ \phi_{\theta\theta}^+$ drops from $y^+ = 16$ at $Pr = 0.71$ to $y^+ = 5$ at $Pr = 7.5$, as the conductive sublayer thins with increasing Prandtl number (Alcántara-Ávila & Hoyas 2021; Kader 1981; Schwertfirm & Manhart 2007). The y^+ location of the peak in $k_z^+ \phi_{\theta\theta}^+$ scales with approximately $Pr^{-1/2}$, which is steeper than the scaling of approximately $Pr^{-1/3}$ for the conductive sublayer thickness for $Pr \gtrsim 1$ (Shaw & Hanratty 1977; Kader 1981; Schwertfirm & Manhart 2007; Alcántara-Ávila & Hoyas 2021; Pirozzoli 2023). We also analysed the $\overline{\theta^2}^+$ profiles of Pirozzoli (2023) for the DNS of the turbulent pipe flow at $Re_{\tau_0} \simeq 1100$ and $Pr = 0.5, 1, 2, 4, 16$, and the y^+ locations of their inner peaks scale with approximately $Pr^{-1/2}$.

For the plane oscillation, we expect that the maximum DR and HR is achieved when the actuation period is close to \mathcal{T}_u^+ and \mathcal{T}_θ^+ , respectively. For the travelling wave, however, the optimal actuation period cannot be directly compared with \mathcal{T}_u^+ or \mathcal{T}_θ^+ , owing to the relative streamwise motion between the travelling wave and the advecting near-wall scales. As discussed by Quadrio *et al.* (2009), for maximum DR, \mathcal{T}_u^+ must be compared with a relative oscillation period $2\pi/(\kappa_x^+ U_u^+ + \omega^+)$ as seen by an observer travelling with the convection speed of the near-wall energetic velocity scales U_u^+ . Similarly, for maximum HR, \mathcal{T}_θ^+ must be compared with $2\pi/(\kappa_x^+ U_\theta^+ + \omega^+)$, where U_θ^+ is the convection speed of the near-wall energetic temperature scales. After some recasting (using $\mathcal{T}_u^+ \simeq \mathcal{T}_\theta^+ \simeq 100$, $\kappa_x^+ = 0.0014$), we estimate the optimum frequencies of actuation for DR and HR to be, respectively,

$$\omega_{\text{opt,DR}}^+ = \frac{2\pi}{\mathcal{T}_u^+} - \kappa_x^+ U_u^+ \simeq 0.046, \quad (3.1a)$$

$$\omega_{\text{opt,HR}}^+ = \frac{2\pi}{\mathcal{T}_\theta^+} - \kappa_x^+ U_\theta^+ \simeq 0.063 - 0.0014 U_\theta^+, \quad (3.1b)$$

where we have assumed that U_u^+ follows a universal curve (Kim & Hussain 1993; Del Álamo & Jiménez 2009; Liu & Gayme 2020), where $U_u^+ \simeq 12$ at $y^+ \simeq 15$ (marked with blue bullets in figure 7*d-i*).

The estimated optimum frequency for DR is independent of Prandtl number, at approximately 0.046, consistent with our DNS results for the travelling wave case (figure 5*a,c,e*). However, the optimum frequency for HR depends on Pr , since we expect that U_θ^+ decreases as the energetic temperature scales move closer to the wall with increasing Prandtl number (red bullets in figure 7*d-i*). Hetsroni *et al.* (2004) computed the profiles of U_θ^+ at $Pr = 1.0, 5.4$ and 54 in a configuration similar to that used in the present study, without actuation. Using their results, we estimate that U_θ^+ decreases from 12 to 6 as Pr increases from 0.71 to 7.5, which gives $\omega_{\text{opt,HR}}^+ = 0.046$ at $Pr = 0.71$ and 0.055 at $Pr = 7.5$. The estimated value at $Pr = 7.5$ is smaller than the value of 0.088 given by the DNS (figure 5*e*), but the trends with Prandtl number are consistent. In §§ 3.6 and 3.7 we conduct a more quantitative justification for the trends in $\omega_{\text{opt,HR}}^+$ by considering the interaction between the Stokes layer and the near-wall thermal field.

3.3. Mean profiles and turbulence statistics

We now consider the distributions of the mean velocity \overline{U}^* ($= \overline{U}/u_\tau$), the mean temperature $\overline{\Theta}^*$ ($= \overline{\Theta}/\theta_\tau$) (figure 8), and the velocity and temperature statistics (figure 9) as we vary ω^+ and Pr . We focus on the travelling wave case, but since the observed trends

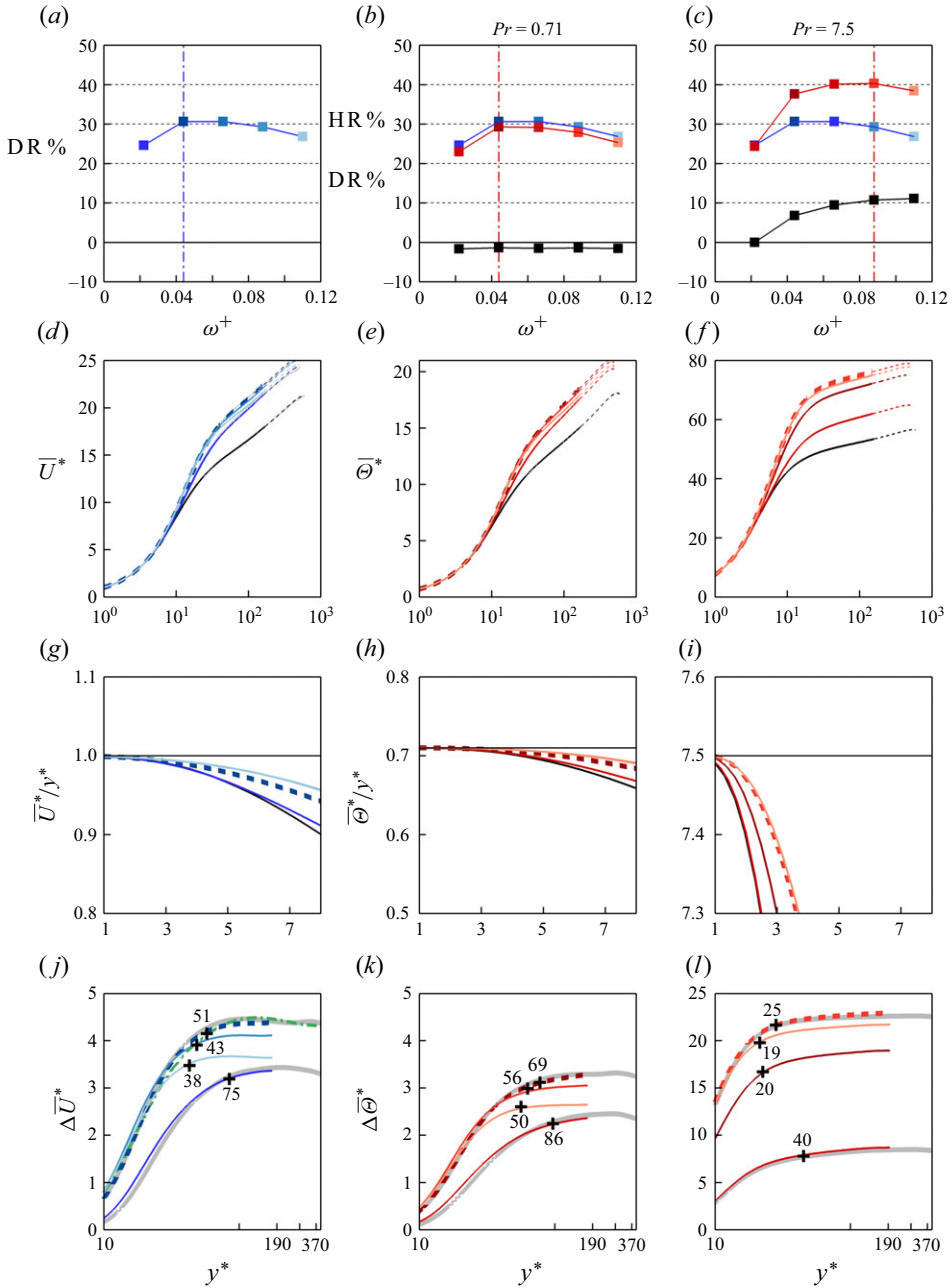


Figure 8. Travelling wave actuation with $A^+ = 12$, $\kappa_x^+ = 0.0014$. Left column: DR % and \overline{U}^* profiles, where $\Delta\overline{U}^* = \overline{U}^* - \overline{U}_0^*$ (results independent of Pr). Middle and right columns correspond to $Pr = 0.71$ and 7.5 , respectively: DR % (blue line), HR % (red line) and $\overline{\Theta}^*$ profiles, where $\Delta\overline{\Theta}^* = \overline{\Theta}^* - \overline{\Theta}_0^*$. In the panels (d–i) the black line is the reference (non-actuated) case, the blue and red lines show the effects of increasing ω^+ on \overline{U}^* and $\overline{\Theta}^*$, respectively, and the thick dashed line corresponds to DR_{max} or HR_{max} . In (d, e, f) the thin dotted lines for $y^* \gtrsim 170$ are the reconstructed profiles following § 2.3. In (j, k, l) we plot the reduced-domain profiles (red/blue) up to $y_{res}^* \simeq 170$, and the thick grey profiles are from the full-domain cases ($L_x \times L_z = 7.6h \times \pi h$) from Appendix A; the dashed-dotted green profile in (j) is at matched $A^+ = 12$, $\kappa_x^+ = 0.0014$, $\omega^+ = 0.044$ but at $Re_{\tau_0} = 950$ from Rouhi *et al.* (2023). The black cross symbols mark the distance y^* where $\Delta\overline{U}^* = 0.9\Delta\overline{U}_{170}^*$ ($\Delta\overline{\Theta}^* = 0.9\Delta\overline{\Theta}_{170}^*$).

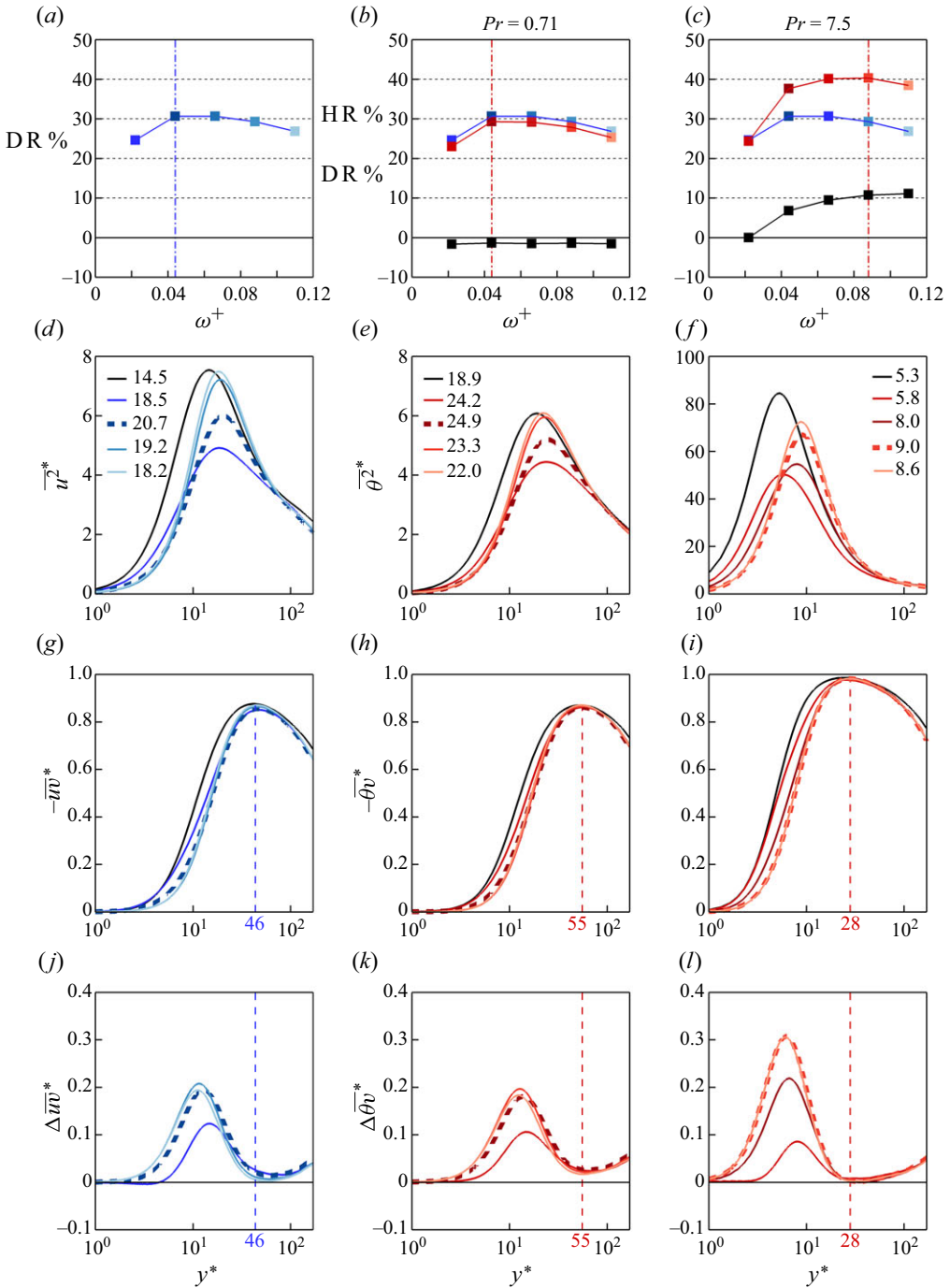


Figure 9. Travelling wave actuation with $A^+ = 12$, $\kappa_x^+ = 0.0014$. Notation and symbols as in figure 8. Here, $\Delta\overline{uv}^* = \overline{uv}^* - \overline{uv}_0^*$ and $\Delta\overline{\theta v}^* = \overline{\theta v}^* - \overline{\theta v}_0^*$. In (d,e,f) the numbers give the y^* location of the inner peak in the $\overline{u^2}^*$ and $\overline{\theta^2}^*$ profiles. In (g-l) the vertical dashed line locates the peak of non-actuated \overline{uv}_0^* (g,j) and $\overline{\theta v}_0^*$ (h,i,k,l).

are consistent with those from the plane oscillation case (figures 28 and 29 in Appendix C), our conclusions are applicable to both types of actuation.

It is well known from the literature that DR by either plane oscillation or a travelling wave coincides with the thickening of the viscous sublayer (Choi *et al.* 1998; Choi & Clayton 2001; Choi 2002; Di Cicca *et al.* 2002; Toubert & Leschziner 2012; Hurst *et al.* 2014; Gatti & Quadrio 2016; Chandran *et al.* 2023; Rouhi *et al.* 2023). This is evident also from our \bar{U}^*/y^* profiles (figure 8g), where the actuated profiles (blue profiles) depart from unity farther from the wall compared with the non-actuated profile (black profile). The conductive sublayer also thickens with wall oscillation, but it then thins substantially with increasing Prandtl number, so that at $Pr = 7.5$ the conductive sublayer is substantially thinner than the viscous sublayer (figure 8i).

Viscous sublayer and conductive sublayer thickening due to the wall oscillation shifts the \bar{U}^* and $\bar{\Theta}^*$ profiles. This is shown in figure 8(j,k,l) where we plot the differences $\Delta\bar{U}^* = \bar{U}^* - \bar{U}_0^*$ and $\Delta\bar{\Theta}^* = \bar{\Theta}^* - \bar{\Theta}_0^*$ between the actuated and non-actuated cases. The cases with the maximum DR (or HR) have the highest $\Delta\bar{U}^*$ (or $\Delta\bar{\Theta}^*$), as highlighted by the thick dashed line in the plots. The profiles in colour are from the production runs with the reduced domain (table 1), and are plotted up to $y_{res}^* \simeq 170$. As a reference, the profiles in grey are from the full-domain cases from Appendix A. There is a good agreement between the reduced-domain and full-domain profiles up to y_{res}^* . Furthermore, the variations of $\Delta\bar{U}^*$ and $\Delta\bar{\Theta}^*$ beyond y_{res}^* are within 3%. Therefore, it is reasonable to consider $\Delta\bar{U}^*$ and $\Delta\bar{\Theta}^*$ at $y_{res}^* = 170$ ($\Delta\bar{U}_{170}^*$ and $\Delta\bar{\Theta}_{170}^*$) as their asymptotic values. According to Rouhi *et al.* (2023), the distance y^* where $\Delta\bar{U}^*$ reaches a plateau indicates the extent to which the Stokes layer disturbs the \bar{U}^* profile. In figure 8(j,k,l), therefore, we mark each profile at the y^* location where $\Delta\bar{U}^* = 0.9\Delta\bar{U}_{170}^*$ ($\Delta\bar{\Theta}^* = 0.9\Delta\bar{\Theta}_{170}^*$). For the present profiles with fixed Re_{τ_0} , A^+ and κ_x^+ , the distance to reach the plateau in $\Delta\bar{\Theta}^*$ depends on ω^+ and Pr (compare figures 8k and 8l), where the plateau is reached at a lower y^* with increasing Prandtl number. We expect that the $\Delta\bar{\Theta}^*$ profiles and the distances to their plateaus would also depend on A^+ and κ_x^+ , but not on Re_{τ_0} . Our conjecture is based on the behaviour of its analogue $\Delta\bar{U}^*$ (figure 8j) that, for a fixed set of actuation parameters, is almost identical between $Re_{\tau_0} = 590$ (thick blue dashed line) and $Re_{\tau_0} = 950$ (green dashed-dotted line). The Reynolds number independence of the plateau in $\Delta\bar{U}^*$ for the travelling wave is further confirmed by Gatti & Quadrio (2016) and Gatti *et al.* (2024).

In figure 9 we plot the turbulence statistics for the same cases shown in figure 8. Drag reduction and viscous sublayer thickening (figure 8a,d,g) coincide with the near-wall attenuation of $\overline{u^{2*}}$ and the shift in its inner peak (figure 9d), as known from previous work (Quadrio & Sibilla 2000; Ricco & Wu 2004; Quadrio & Ricco 2011; Toubert & Leschziner 2012; Ricco *et al.* 2021; Rouhi *et al.* 2023). Similarly, we find that at each Pr , HR and conductive sublayer thickening (figure 8b,c,e,f,h,i) coincide with the near-wall attenuation of $\overline{\theta^{2*}}$ and the shift in its inner peak (figure 9e,f). Interestingly, DR_{max} occurs when the inner peak in $\overline{u^{2*}}$ is located farthest from the wall, and a similar connection exists between HR_{max} and the location of the inner peak in $\overline{\theta^{2*}}$ (compare the listed numbers in figure 9d,e,f).

In addition, the attenuation of the turbulent shear stress $\overline{uv^*}$ (figure 9g) and the wall-normal turbulent temperature flux $\overline{\theta v^*}$ (figure 9h,i) are directly linked to DR and HR,

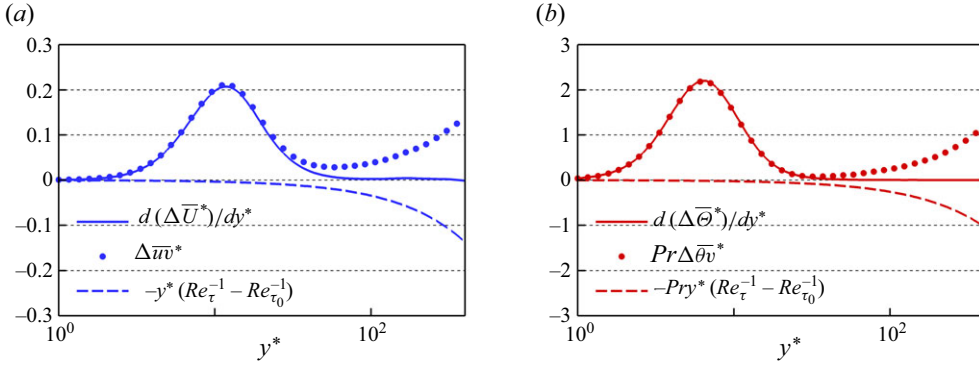


Figure 10. Travelling wave actuation with $A^+ = 12$, $\kappa_x^+ = 0.0014$, $\omega^+ = 0.088$ at $Pr = 7.5$. (a) Terms in the averaged streamwise momentum equation (3.3a). (b) Terms in the averaged temperature equation (3.3b).

respectively. In figure 9(j,k,l) we plot the differences between the actuated and non-actuated cases $\Delta\bar{u}v^* = \bar{u}v^* - \bar{u}v_0^*$ and $\Delta\bar{\theta}v^* = \bar{\theta}v^* - \bar{\theta}v_0^*$. Most of the attenuation occurs near the wall, with the maxima occurring near $y^* \simeq 10$. For $y^* > 10$, the attenuation declines, and $\Delta\bar{u}v^*$ and $\Delta\bar{\theta}v^*$ reach local minima at points that coincide approximately with the locations of the peaks in $\bar{u}v_0^*$ and $\bar{\theta}v_0^*$.

By integrating the plane- and time-averaged streamwise momentum (2.2) and temperature (2.3) equations from zero to y^* , we obtain

$$\frac{d\bar{U}^*}{dy^*} = \bar{u}v^* + (1 - y^* Re_\tau^{-1}), \quad \frac{d\bar{\Theta}^*}{dy^*} = Pr \left[\bar{\theta}v^* + (1 - y^* Re_\tau^{-1}) + Res_\Theta \right], \quad (3.2a,b)$$

where $Res_\Theta \equiv Re_\tau^{-1} \int_0^{y^*} (1 - \bar{U}^*/U_b^*) dy'$. Hence,

$$\frac{d(\Delta\bar{U}^*)}{dy^*} = \Delta\bar{u}v^* - y^* (Re_\tau^{-1} - Re_{\tau_0}^{-1}), \quad (3.3a)$$

$$\frac{d(\Delta\bar{\Theta}^*)}{dy^*} = Pr \left[\Delta\bar{\theta}v^* - y^* (Re_\tau^{-1} - Re_{\tau_0}^{-1}) + \underbrace{\Delta Res_\Theta}_{\simeq 0} \right]. \quad (3.3b)$$

The difference ΔRes_Θ between the actuated and non-actuated cases is small and can be neglected. The remaining terms in (3.3a) and (3.3b) are plotted in figure 10 for the travelling wave case at $Pr = 7.5$ and $\omega^+ = 0.088$. We see that the right-hand-side of (3.3a) and (3.3b) are dominated by $\Delta\bar{u}v^*$ and $\Delta\bar{\theta}v^*$, up to their respective minima, but farther from the wall these terms are cancelled by the term containing the difference in Reynolds numbers ($Re_\tau^{-1} - Re_{\tau_0}^{-1}$). That is, the net contributions to $\Delta\bar{U}^*$ and $\Delta\bar{\Theta}^*$, hence, DR and HR, come from $\Delta\bar{u}v^*$ and $\Delta\bar{\theta}v^*$, and then only up to the points where $\Delta\bar{u}v^*$ and $\Delta\bar{\theta}v^*$ reach their minimum values.

3.4. Source of inequality between HR and DR

Integrating (3.3a) and (3.3b) once more with respect to y^* gives

$$\Delta\bar{U}_{y^*}^* = \int_0^{y^*} \Delta_{uv}^* dy', \quad \Delta\bar{\Theta}_{y^*}^* = Pr \int_0^{y^*} \Delta_{\theta v}^* dy', \quad (3.4a,b)$$

where

$$\Delta_{uv}^* \equiv \Delta \overline{uv}^* - y^*(Re_\tau^{-1} - Re_{\tau_0}^{-1}), \tag{3.4c}$$

$$\Delta_{\theta v}^* \equiv \Delta \overline{\theta v}^* - y^*(Re_\tau^{-1} - Re_{\tau_0}^{-1}). \tag{3.4d}$$

By using (3.4a) we can relate Δ_{uv}^* and $\Delta_{\theta v}^*$ to $\Delta \overline{U}^*$ and $\Delta \overline{\Theta}^*$, hence, to DR and HR, and so establish the connection between the DR and HR and the turbulence attenuation. For the DR, Gatti & Quadrio (2016) derived the relation between DR ($= 1 - R_f$) and the asymptotic value of $\Delta \overline{U}^*$ in the log region (3.5a). In Appendix B we derive a similar relation between HR ($= 1 - R_h$) and the asymptotic value of $\Delta \overline{\Theta}^*$ in the log region (3.5b). That is, we have

$$\Delta \overline{U}_{170}^* = \sqrt{\frac{2}{C_{f_0}}} \left[\frac{1}{\sqrt{R_f}} - 1 \right] - \frac{1}{2\kappa_u} \ln R_f = \underbrace{\int_0^{170} \Delta_{uv}^* dy'}_{I_{uv}}, \tag{3.5a}$$

$$\Delta \overline{\Theta}_{170}^* = \frac{\sqrt{C_{f_0}/2}}{C_{h_0}} \left[\frac{\sqrt{R_f}}{R_h} - 1 \right] - \frac{1}{2\kappa_\theta} \ln R_f = Pr \underbrace{\int_0^{170} \Delta_{\theta v}^* dy'}_{I_{\theta v}}. \tag{3.5b}$$

These derivations assume that the profiles of \overline{U}^* and $\overline{\Theta}^*$ have well-defined log regions with slopes that are not affected by the wall oscillation, which is the case for our results (figure 8). The integration was performed up to $y_{res}^* = 170$, where the profiles of $\Delta \overline{U}^*$ and $\Delta \overline{\Theta}^*$ reach their asymptotic levels (figure 8j,k,l) and their derivatives are zero (figure 10). On the right-hand sides of (3.5a) and (3.5b) we have the integrals of attenuation in the turbulent shear stress (I_{uv}) and the turbulent temperature flux ($I_{\theta v}$). For a fixed set of viscous-scaled actuation parameters, $I_{uv} = \Delta \overline{U}_{170}^*$ is constant (Gatti & Quadrio 2016; Rouhi *et al.* 2023) (also shown in figure 8j), but $I_{\theta v} = \Delta \overline{\Theta}_{170}^*/Pr$ depends on Pr (figure 9k,l).

To predict DR and HR from (3.5a) and (3.5b), we only need $\Delta \overline{U}_{170}^*$ and $\Delta \overline{\Theta}_{170}^*$ (that is, I_{uv} and $I_{\theta v}$) as the inputs; the other parameters are associated with the non-actuated channel flow for which semi-empirical relations exist in the literature. We choose $\kappa_u = 0.4$ and $\kappa_\theta = 0.46$ (Pirozzoli *et al.* 2016); the suitability of these choices is confirmed in § 2.3 and Appendix A. Dean (1978)'s correlation is used for the non-actuated skin-friction coefficient $C_{f_0} = 0.073(2Re_b)^{-1/4}$, which could be re-expressed as $C_{f_0} = 0.037Re_{\tau_0}^{-2/7}$; this correlation agrees well with the DNS data (MacDonald *et al.* 2019), and yields less than 2 % difference with our DNS result $C_{f_0} = 0.0057$ at $Re_{\tau_0} = 590$. For the non-actuated C_{h_0} , in figure 11 we compare our DNS data at $Re_{\tau_0} = 590$ and different Pr (cases on the left side of table 1) with several empirical relations. These relations define C_{h_0} either based on the bulk temperature Θ_b or the mixed-mean temperature Θ_m . For our DNS data, there is a negligible difference between the two definitions (empty versus the filled circles). Among the relations, the latest correlation by Pirozzoli *et al.* (2022) agrees well with our DNS data (solid black line). This relation is an improvement to Kader & Yaglom (1972)'s formula, and its accuracy is supported by the recent DNS of Pirozzoli (2023) for $\mathcal{O}(10^{-2}) \lesssim Pr \lesssim \mathcal{O}(10^1)$. It is formulated as

$$\frac{1}{C_{h_0}} = \frac{\kappa_u}{\kappa_\theta} \frac{2}{C_{f_0}} + \left(\beta_{CL} - \beta_2 - \frac{\kappa_u}{\kappa_\theta} B \right) \sqrt{\frac{2}{C_{f_0}}} + \beta_3. \tag{3.6}$$

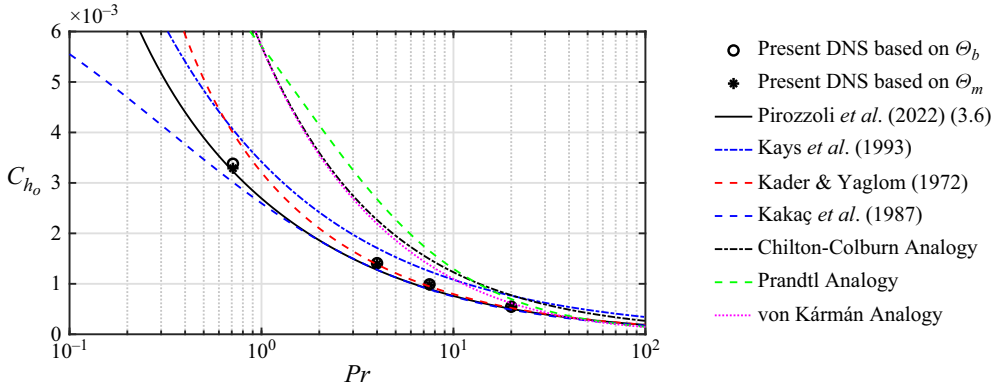


Figure 11. Comparison of the non-actuated C_{h_0} between our DNS cases (left side of table 1) and several empirical relations. For the DNS data, C_{h_0} is calculated either based on the bulk temperature Θ_b (empty symbols) or the mixed-mean temperature Θ_m (filled symbols). The empirical relations are by Pirozzoli *et al.* (2022) (3.6), Kays *et al.* (1993), Kader & Yaglom (1972), Kakaç *et al.* (1987), Chilton–Colburn analogy (Chilton & Colburn 1934; Colburn 1964), Prandtl analogy (see equation 11 in Schlünder 1998) and the von Kármán analogy (see equation 4 in Li & Li 2010).

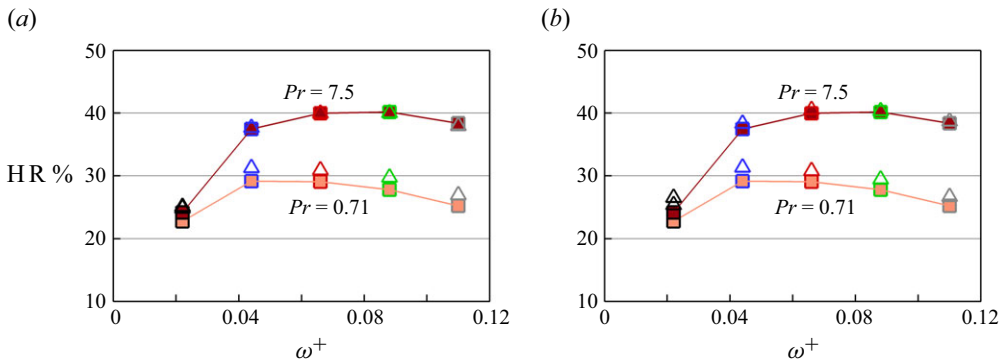


Figure 12. Travelling wave actuation with $A^+ = 12$, $\kappa_x^+ = 0.0014$. Comparison between the direct HR from DNS (filled squares) and the predicted HR (empty triangles) by solving (3.5a) and (3.5b). In (a), for predicting HR, we use I_{uv} and $I_{\theta v}$ directly from DNS. In (b), for predicting HR, we use a power-law estimate for $I_{\theta v} = I_{uv}/Pr^\gamma$, with the values of γ reported in figure 13(b).

Here $\beta_{CL}(Pr) = B_\theta(Pr) + 3.504 - 1.5/\kappa_\theta$, $\beta_2 = 4.92$, $\beta_3 = 39.6$, $B = 1.23$ and $B_\theta(Pr)$ is the log-law additive constant for $\overline{\Theta}^*$ (Kader & Yaglom 1972), as introduced in Appendix B.

In figure 12(a) we compare the values of HR from DNS with those from (3.5a) and (3.5b) using I_{uv} and $I_{\theta v}$ as obtained from DNS. The results support the accuracy of the model for relating HR to the attenuation of the turbulent flux. In figure 12(b) we also show the agreement between the model and the DNS when we use a power-law estimate for $I_{\theta v} (= I_{uv}/Pr^\gamma)$ where only I_{uv} (which is independent of Pr) is obtained from DNS. We justify the power law as follows.

From (3.5b), we note that the Prandtl number dependence of HR (hence HR – DR) is due to both C_{h_0} and $I_{\theta v}$. According to the Reynolds analogy, we would expect $I_{\theta v} = I_{uv}$ when $Pr = 1.0$. Figure 13(a) indicates that, regardless of the actuation frequency ω^+ ,

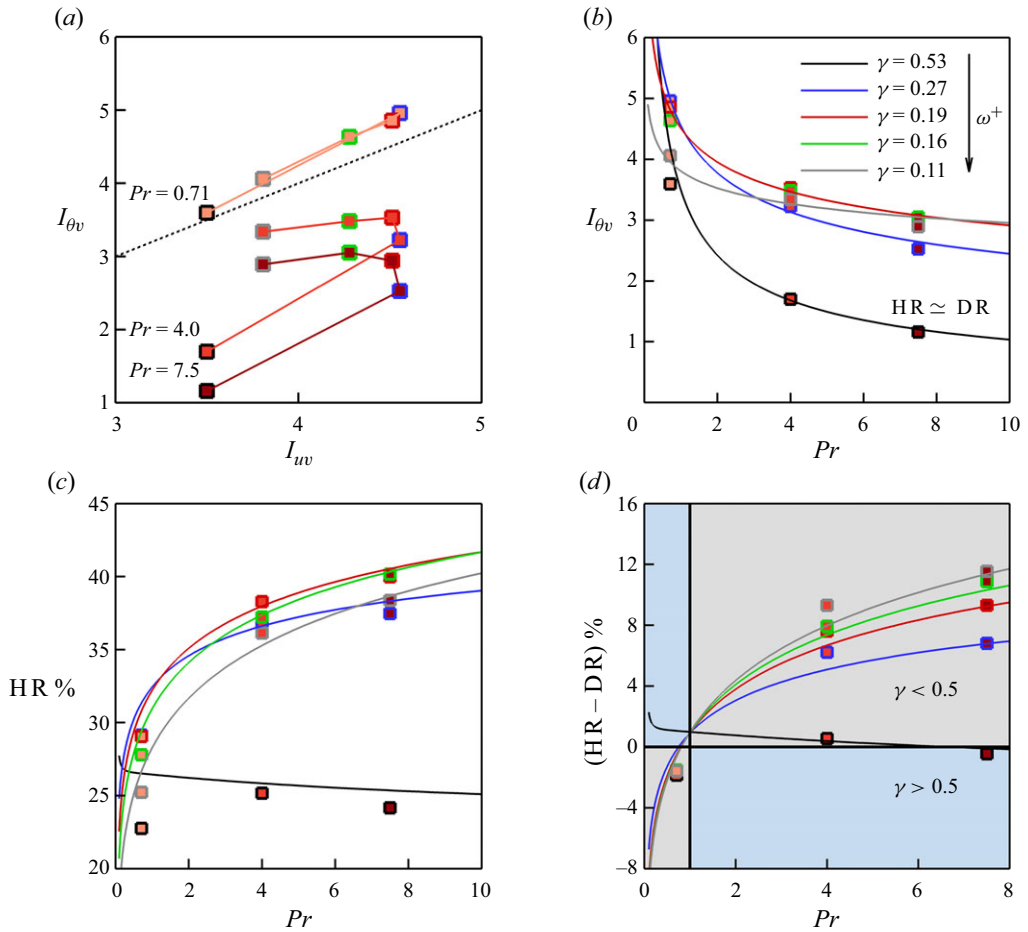


Figure 13. Travelling wave at $Pr = 0.71, 4.0$ and 7.5 (same data as in figure 5a,c,e). The outline colour of each data point indicates its ω^+ ; $\omega^+ = 0.022$ (black), 0.044 (blue), 0.066 (red), 0.088 (green) and 0.110 (grey). (a) Plot of $I_{\theta v}$ versus I_{uv} ; the dotted line is for $I_{\theta v} = I_{uv}$. (b) Plot of $I_{\theta v}$ versus Pr ; the solid curves are the power-law fit $I_{\theta v} = I_{uv}/Pr^\gamma$, with γ as shown. (c,d) Plots of HR and $HR - DR$ versus Pr ; the solid curves are the prediction of (3.5b) using $I_{\theta v} = I_{uv}/Pr^\gamma$. In (d), the blue zone marks $\gamma > 0.5$ and the grey zone marks $\gamma < 0.5$.

$I_{\theta v} > I_{uv}$ for $Pr = 0.71$ and $I_{\theta v} < I_{uv}$ for $Pr > 1$, with the difference increasing with Pr . In other words, increasing Pr beyond unity leads to a lower attenuation of $\overline{\theta v}$ compared with \overline{uv} , even though in this regime $HR > DR$ (figure 5c-f). Figure 13(b) shows how $I_{\theta v}$ depends on Pr , and that $I_{\theta v} = I_{uv}/Pr^\gamma$ is a good approximation to the data. For the present data with a fixed A^+ and κ_x^+ , γ depends on ω^+ but it is independent of Pr . When we use this power law in (3.5b) and solve for HR by using I_{uv} from DNS, figure 13(c,d) shows that the model closely matches the data. Furthermore, for $\gamma < 0.5$, we can achieve $HR > DR$ for $Pr > 1$, and the smaller γ is the higher HR compared with DR. From figure 13(b,d), as ω^+ increases from 0.022 (black curve) to 0.110 (grey curve), γ decreases from approximately 0.5 to 0.1 , and $HR - DR$ increases from almost zero to 10% . Therefore, we expect $HR < DR$ for $Pr > 1.0$ if $\gamma > 0.5$. This occurs for the plane oscillation at $\omega^+ = 0.022$, where $\gamma = 2.43$ and $HR - DR \simeq -5\%$ (figure 21).

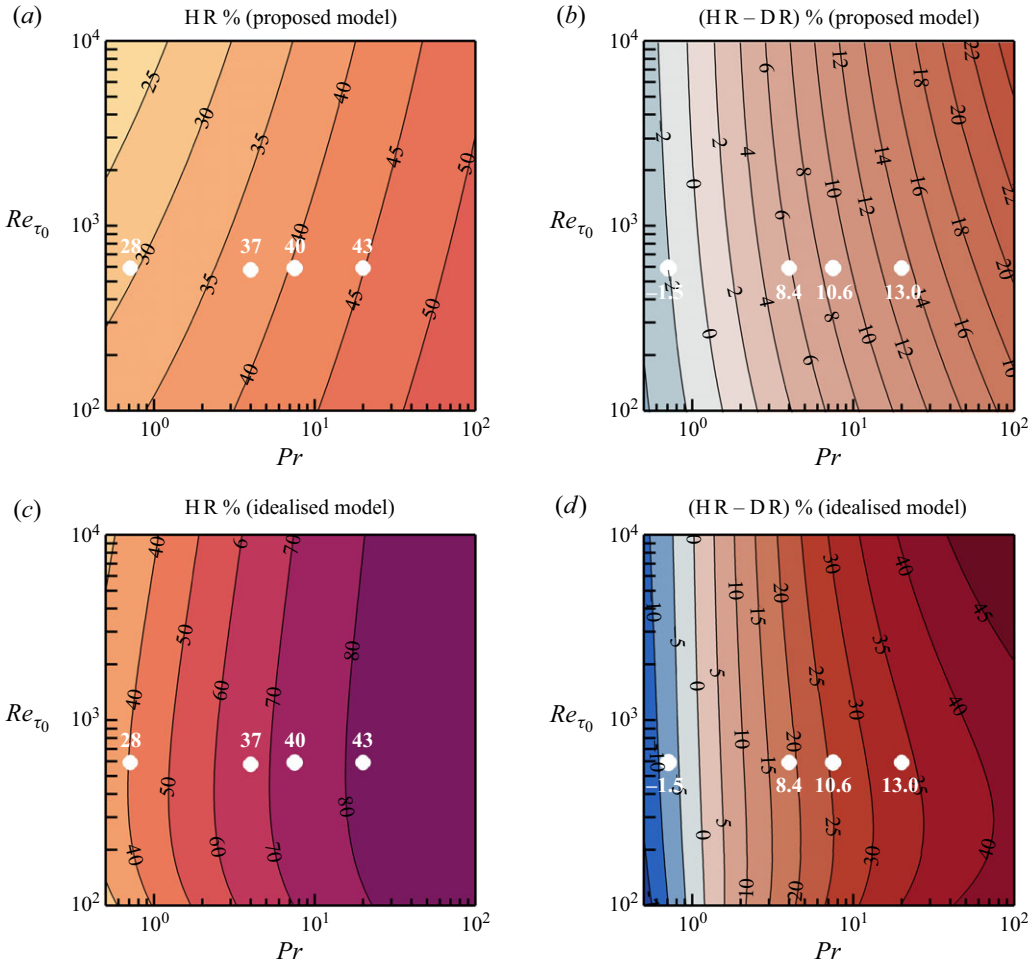


Figure 14. Predicted maps of (a,c) HR and (b,d) HR – DR for the travelling wave with $A^+ = 12$, $\kappa_x^+ = 0.0014$ and $\omega^+ = 0.088$. Plots (a,b) are obtained from our proposed model $I_{\theta v} = I_{uv}/Pr^\gamma$ with $I_{uv} = 4.28$, $\gamma = 0.16$ obtained from DNS, and by solving (3.5a, 3.5b). Plots (c,d) are obtained from the simplified model (3.7a, 3.7b) and by solving (3.5a, 3.5b). The white bullets represent DNS results at $Re_{\tau_0} = 590$ for $Pr = 0.71, 4.0, 7.5$ and 20.

3.5. Heat-transfer reduction at higher Prandtl number and Reynolds number

Gatti & Quadrio (2016) used (3.5a) to extrapolate their low-Reynolds-number DR data to higher Reynolds numbers, and the accuracy of this extrapolation was corroborated by Rouhi *et al.* (2023) up to $Re_{\tau_0} = 4000$ using LES and by Gatti *et al.* (2024) up to $Re_{\tau_0} = 6000$ using DNS. For a fixed set of actuation parameters (A^+ , κ_x^+ , ω^+), I_{uv} is Reynolds and Prandtl number independent, and so the only Reynolds number dependency of DR is through C_{f_0} . Hence, Gatti & Quadrio (2016) could solve (3.5a) and predict DR at any Reynolds number. We can now do the same for HR by using the power-law relationship $I_{\theta v} = I_{uv}/Pr^\gamma$. By knowing I_{uv} and γ for a fixed set of actuation parameters, we can then solve (3.5a) and (3.5b) to map HR and HR – DR as functions of Pr and Re_{τ_0} .

In figure 14(a,b) we show these predictions for the travelling wave case with $\omega^+ = 0.088$, where the DNS gives $I_{uv} = 4.28$ and $\gamma = 0.16$ (data points with green outline in figure 13). The predictions agree well with the DNS data points, including the point

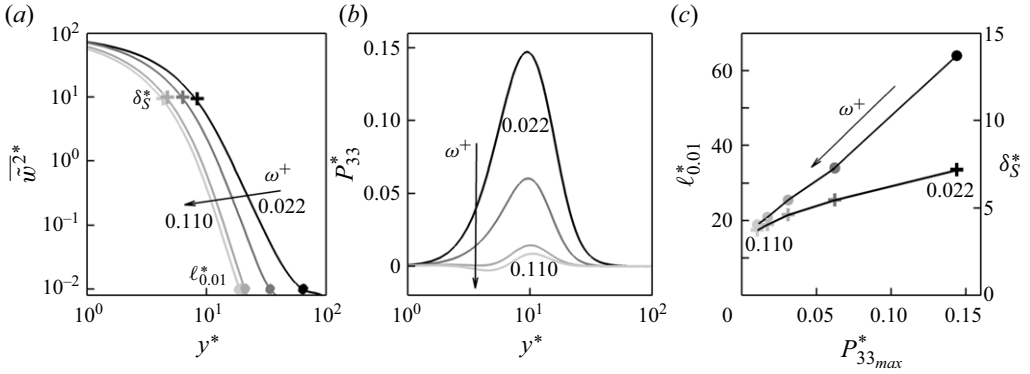


Figure 15. Characteristics of the Stokes layer for the travelling wave with $A^+ = 12$, $\kappa_x^+ = 0.0014$ and $0.022 \leq \omega^+ \leq 0.110$ (same cases as in figure 5a,c,e). Results are independent of Prandtl number. The colour of the profiles and data points change from black at $\omega^+ = 0.022$ to light grey at $\omega^+ = 0.110$. (a) Profiles of \bar{w}^{2*} . Stokes layer protrusion height $\ell_{0.01}^*$ (Rouhi *et al.* 2023) marked at $\bar{w}^{2*} = 0.01$ (filled bullets); laminar Stokes layer thickness δ_s^* marked at $\bar{w}^{2*} = (1/2)A^{*2}e^{-2}$ (cross symbols). (b) Production due to the Stokes layer P_{33}^* . (c) Plot of $\ell_{0.01}^*$ (filled bullets) and δ_s^* (cross symbols) versus the maximum value of \tilde{P}_{33}^* .

at $Pr = 20$ (HR = 43 %, HR – DR = 13 %) (see table 1). At a given Reynolds number, HR increases almost logarithmically with Prandtl number. For instance, at $Re_{\tau_0} = 590$ HR increases from 30 % to 40 % as the Prandtl number increases from 0.71 to 7.5, and HR = 50 % would be obtained at a Prandtl number of approximately 75. In addition, HR decreases very slowly with increasing Re_{τ_0} . For instance, at $Pr = 7.5$ HR decreases from 40 % to approximately 36 % as Re_{τ_0} increases from 590 to 5900. Such a slow decrease with Re_{τ_0} is similarly observed in the predictive model for DR (3.5a) (Marusic *et al.* 2021; Rouhi *et al.* 2023; Gatti *et al.* 2024).

In figure 14(c,d) we predict HR and HR – DR for the same actuated case as in figure 14(a,b), but with a simplified analytical approach, similar to that proposed by Iwamoto *et al.* (2005). The approach assumes that turbulence is completely damped in the near-wall region, which here we consider that to be up to the Stokes layer protrusion height $\ell_{0.01}^*$ (figure 15a). Therefore, for $0 \leq y^* \leq \ell_{0.01}^*$, the profiles are assumed to be laminar $\bar{U}^* = y^*[1 - y^*/(2Re_\tau)]$, $\bar{\Theta}^* = Pr y^*[1 - y^*/(2Re_\tau)]$, and for $y^* > \ell_{0.01}^*$, the profiles follow the turbulent formulations (C1a), (C1b). By matching the laminar and turbulent profiles at $y^* = \ell_{0.01}^*$, we obtain

$$\Delta \bar{U}_{170}^* = \ell_{0.01}^* \left(1 - \frac{\ell_{0.01}^*}{2Re_\tau} \right) - \left(\frac{1}{\kappa_u} \ln \ell_{0.01}^* + B_u \right), \tag{3.7a}$$

$$\Delta \bar{\Theta}_{170}^* = Pr \ell_{0.01}^* \left(1 - \frac{\ell_{0.01}^*}{2Re_\tau} \right) - \left(\frac{1}{\kappa_\theta} \ln \ell_{0.01}^* + B_\theta \right). \tag{3.7b}$$

We substitute for $\Delta \bar{U}_{170}^*$, $\Delta \bar{\Theta}_{170}^*$ in (3.5a), (3.5b) to predict HR and HR – DR. With this approach, the predicted HR and HR – DR increase with Pr (figure 14c,d), consistent with our proposed model and DNS (figure 14a,b). However, quantitatively, this approach overpredicts HR and HR – DR by two times compared with the DNS data and our proposed model, which is of no surprise. The Stokes layer does not completely attenuate the near-wall turbulence, even down to $y^* \sim \mathcal{O}(1)$ (figure 9). The level of attenuation results from the complex interaction between the Stokes layer and the near-wall velocity and thermal fields, as we discuss next.

3.6. Stokes layer interaction with the velocity and thermal fields: integral parameters

For $Re_{\tau_0} \lesssim \mathcal{O}(10^3)$, the primary source of DR is the protrusion of the Stokes layer due to the wall oscillation that modifies the near-wall velocity field (Choi *et al.* 1998; Choi & Clayton 2001; Choi 2002; Choi *et al.* 2002; Quadrio & Sibilla 2000; Ricco 2004; Quadrio & Ricco 2011; Ricco *et al.* 2021), and we would expect that a similar interaction between the Stokes layer and the near-wall temperature field leads to HR. As a result, the near-wall $\overline{u^2}^*$ profiles are modified (figure 9d), consistent with the literature (Jung *et al.* 1992; Baron & Quadrio 1995; Choi *et al.* 1998; Quadrio & Sibilla 2000; Choi & Clayton 2001; Ricco & Wu 2004; Quadrio & Ricco 2011; Touber & Leschziner 2012; Ricco *et al.* 2012; Rouhi *et al.* 2023), and similar trends are seen in the $\overline{\theta^2}^*$ profiles (figure 9e,f). To determine how the Stokes layer affects I_{uv} and $I_{\theta v}$ as the Prandtl number changes, we first identify the Stokes layer characteristics through the harmonic component of the spanwise velocity \tilde{w}^2 , where \tilde{w} is obtained by applying triple decomposition:

$$W(x, y, z, t) = \overline{W}(y) + \tilde{w}(x, y, t) + w(x, y, z, t), \tag{3.8a}$$

$$\tilde{w}(x, y, t) = \underbrace{\frac{1}{N} \sum_{n=0}^{N-1} W(x, y, t + nT_{osc}) - \overline{W}(y)}_{\langle W \rangle(x, y, t)}. \tag{3.8b}$$

Here, \overline{W} is the plane- and time-averaged component of the spanwise velocity, \tilde{w} is the harmonic component, w is the turbulent component and $\langle W \rangle$ is the spanwise- and phase-averaged value of W . For the streamwise and wall-normal velocities and the temperature field, the harmonic components are negligible compared with the turbulent components. Following Rouhi *et al.* (2023), we quantify the Stokes layer protrusion height $\ell_{0.01}^*$ as the wall distance where $\overline{w^2}^* = 0.01$, and we locate the Stokes layer thickness δ_S^* where $\overline{w^2}^* = (1/2)A^{*2}e^{-2}$. We also calculate the production due to the Stokes layer according to $P_{33}^* \equiv -2\langle wv \rangle \partial \tilde{w} / \partial y^* - 2\langle wu \rangle \partial \tilde{w} / \partial x^*$, where P_{33}^* is the only external source term due to the Stokes layer that injects energy into the turbulent stress budgets (Touber & Leschziner 2012; Umair *et al.* 2022).

The behaviour of these Stokes layer parameters is given in figure 15 for the same travelling wave cases shown in figure 5(a,c,e). The profiles do not depend on Pr , that is, at a fixed ω^+ the Stokes layer structure remains unchanged as the Prandtl number changes. When ω^+ decreases, $\ell_{0.01}^*$ and the maximum production increase proportionately (figure 15c). In other words, the Stokes layer becomes more protrusive while injecting more energy into the turbulent field. We note that $\ell_{0.01}^*$ is almost linearly proportional to P_{33max}^* , but δ_S^* is less responsive to the rise in the production. Therefore, $\ell_{0.01}^*$ better quantifies the Stokes layer protrusion and strength, as sensed by the turbulent field, in agreement with the observations by Rouhi *et al.* (2023).

In figure 16 we assess the relation between the integral quantities DR, HR, $I_{\theta v}$, I_{uv} and the Stokes layer characteristics. Rouhi *et al.* (2023) showed that DR increases with $\ell_{0.01}^*$ up to an optimal value for maximum DR, corresponding to an optimal level of P_{33max}^* . For our present cases, this optimal point is $\ell_{0.01}^* = 34$ (figure 16b), where protrusion beyond this point causes DR to decrease. We observe a similar trend in HR (figure 16b), but the corresponding optimal value of $\ell_{0.01}^*$ for maximum HR decreases from 34 to 21 as the Prandtl number increases from 0.71 to 7.5. Figure 16(c,d) shows that the variations of I_{uv} and $I_{\theta v}$ with ω^+ and $\ell_{0.01}^*$ are consistent with the trends in DR and HR. In terms of

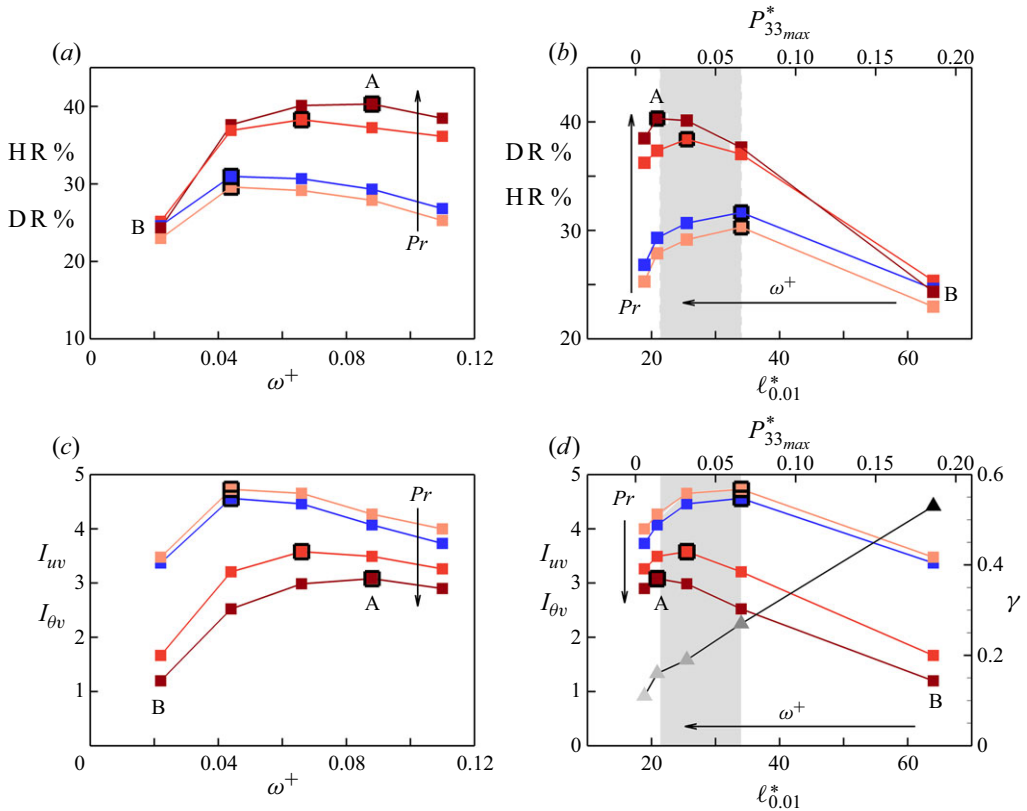


Figure 16. Variation of the integral parameters with the Stokes layer characteristics ($\ell_{0.01}^*$, P_{33max}^*) for the same travelling wave cases as in figure 15. Plot (a) shows DR (blue squares), HR (light orange to brick red squares) versus ω^+ . (b) Same data as in (a) versus $\ell_{0.01}^*$ (bottom axis) and P_{33max}^* (top axis). Plots (c,d) correspond to (a,b) for I_{uv} (blue squares) and $I_{\theta v}$ (light orange to brick red squares); in (d) we overlay γ (grey to black triangles). In all plots, the colour of HR and $I_{\theta v}$ changes from light orange at $Pr = 0.71$ to brick red at $Pr = 7.5$. The points associated with DR_{max} and HR_{max} are highlighted with a larger symbol size and black outline. In (b,d) the grey region shades the range of DR_{max} and HR_{max} . In all plots we highlight two cases that we further analyse in figures 17 and 18: case A at $\omega^+ = 0.088$ with $\gamma = 0.16$ and case B at $\omega^+ = 0.022$ with $\gamma = 0.53$.

variations with Pr , however, HR increases even as $I_{\theta v}$ decreases. From $Pr = 0.71$ to 7.5 , the maximum value of $I_{\theta v}$ shifts to smaller values of $\ell_{0.01}^*$, corresponding to a shift in ω^+ from 0.044 ($\ell_{0.01}^* = 34$) to 0.088 ($\ell_{0.01}^* = 21$). Finally, it appears that the exponent γ in the power law increases almost linearly with $\ell_{0.01}^*$ and P_{33max}^* (figure 16d).

To summarise, we find that for $Pr > 1$, achieving maximum HR requires a less protrusive Stokes layer than achieving maximum DR. As the Stokes layer becomes more protrusive (energetic), it loses its efficacy in attenuating $\overline{\theta v}^*$ relative to \overline{uv}^* , that is, γ increases as $\ell_{0.01}^*$ increases.

3.7. Stokes layer interaction with the velocity and thermal fields: scale-wise analysis

To better understand our observations on the integral parameters shown in figure 16, we now examine the spectrograms of \overline{uv}^* and $\overline{\theta v}^*$ and visualise the distributions of the instantaneous uv and θv near the wall. We focus on two cases at $Pr = 7.5$, case A at $\omega^+ = 0.088$, where HR is maximum and DR is near maximum ($\gamma = 0.16$), and case B

at $\omega^+ = 0.022$, where HR and DR drop below their maximum values, owing to a highly protrusive Stokes layer ($\gamma = 0.53$).

Figure 17 displays the various pre-multiplied spectrograms for these two cases, where ϕ is the spectral density, k_x is the streamwise wavenumber, k_z is the spanwise wavenumber and f is the frequency. The differences between the actuated and non-actuated cases are denoted by, for example, $\Delta k_x^* \phi_{uv}^* = k_x^* \phi_{uv}^* - k_x^* \phi_{uv0}^*$. The extent up to which $\Delta k_x^* \phi_{uv}^*$ and $\Delta k_x^* \phi_{\theta v}^*$ are non-zero (red and blue fields in figure 17*e,f,q,r*) coincides with the height of the Stokes layer protrusion $\ell_{0,01}^*$ (horizontal dashed line); this supports the robustness of $\ell_{0,01}^*$ to measure the extent up to which the Stokes layer modifies the turbulent field. Overall, for both cases A and B, and $k_x^* \phi_{uv}^*$ and $k_x^* \phi_{\theta v}^*$, the Stokes layer protrusion (production) leads to two outcomes: (i) large-scale energy attenuation as a favourable outcome (positive $\Delta k_x^* \phi_{uv}^*$, $\Delta k_x^* \phi_{\theta v}^*$ for $\lambda_x^* \gtrsim 350$, shown as the red fields in figure 17*e,f,q,r*), and (ii) small-scale energy amplification as an unfavourable outcome (negative $\Delta k_x^* \phi_{uv}^*$, $\Delta k_x^* \phi_{\theta v}^*$ for $\lambda_x^* \lesssim 350$, shown as the blue fields). The large-scale energy attenuation corresponds to the attenuation of the near-wall streaks with $\lambda_x^* \simeq 10^3$ (see the energetic peaks in the non-actuated spectrograms). The small-scale energy amplification corresponds to the emergence of smaller scales with $\lambda_x^* \simeq 10^2$ (figure 18*j,k,l,m,u,v,w,x*). The drastic changes in the streamwise spectrograms (figure 17*e,f,q,r*) are echoed in the response of the frequency spectrograms (figure 17*g,h,s,t*). Changing the actuation frequency ω^+ , hence changing the Stokes layer time scale, modifies the near-wall turbulence time scale T^* , which in turn modifies the streamwise length scale λ_x^* (of course, T^* is related to λ_x^* through a convection speed of approximately $\mathcal{O}(10)$ according to Taylor's hypothesis).

Further insight can be gained by comparing the near-wall instantaneous fields of u^*v^* and θ^*v^* , as shown in figure 18. The response of u^*v^* to the Stokes layer (blue intensity fields) largely follows the trends seen in $\Delta k_x^* \phi_{uv}^*$ and $\Delta f^* \phi_{uv}^*$. For case A, we see that the large scales associated with the near-wall streaks are attenuated. At the same time, sparse patches of smaller scales with $\lambda_x^* \simeq 10^2$ ($T^* \simeq 10$) emerge. For case B, the emerging smaller scales possess a similar structure and size to those in case A, but with a noticeably larger population; they appear as large and closely spaced patches that cover a significant area of the near-wall region. Consistently, negative regions of $\Delta k_x^* \phi_{uv}^*$ and $\Delta f^* \phi_{uv}^*$ are small for case A (figure 17*e,g*), and large for case B (figure 17*q,s*). Thus, I_{uv} and DR are greater for case A than for case B (figure 16). Attenuation of the large scales associated with the near-wall streaks is considered to be a primary source of DR, as extensively reported in the literature (Baron & Quadrio 1995; Di Cicca *et al.* 2002; Karniadakis & Choi 2003; Ricco 2004; Quadrio *et al.* 2009; Toubert & Leschziner 2012; Ricco *et al.* 2021; Marusic *et al.* 2021; Rouhi *et al.* 2023). However, amplification of the smaller scales as a source of drag increase, is reported to a lesser extent. Toubert & Leschziner (2012) observed such amplification in the frequency spectrograms $f^* \phi_{uu}^*$, $f^* \phi_{vv}^*$ and $f^* \phi_{ww}^*$. Consistent with our figure 17, they noted that as ω^+ changes from 0.06 to 0.03, and the Stokes layer production (protrusion) increases, energy accumulates in the scales with $T^* \simeq 10$ and DR decreases. Similarly, energy amplification at $T^* \simeq 10$ is observed in $f^* \phi_{\tau\tau}^*$ by Chandran *et al.* (2023), and in the near-wall $f^* \phi_{uu}^*$ by Deshpande *et al.* (2023).

As to the θ^*v^* field (brick intensity fields in figure 18), we see that with $Pr > 1.0$ the Stokes layer modifies the θ^*v^* field more than the u^*v^* field. In case A, for example, the scales with $\lambda_x^* \simeq 10^2$ and $T^* \simeq 10$ are more frequent and more densely populated in the θ^*v^* fields (figure 18*l,m,r,s*) than in the u^*v^* fields (figure 18*j,k,p,q*). Consistently, $\Delta k_x^* \phi_{\theta v}^*$ (figure 17*f*) is more positive than $\Delta k_x^* \phi_{uv}^*$ (figure 17*e*) for $\lambda_x^* \gtrsim 350$, and more negative for $\lambda_x^* \lesssim 350$. We can make the same observations with respect to case B (figure 17*q,r*). As a result, at each ω^+ , $I_{\theta v}$ falls below I_{uv} when $Pr > 1$ (figure 16*c,d*).

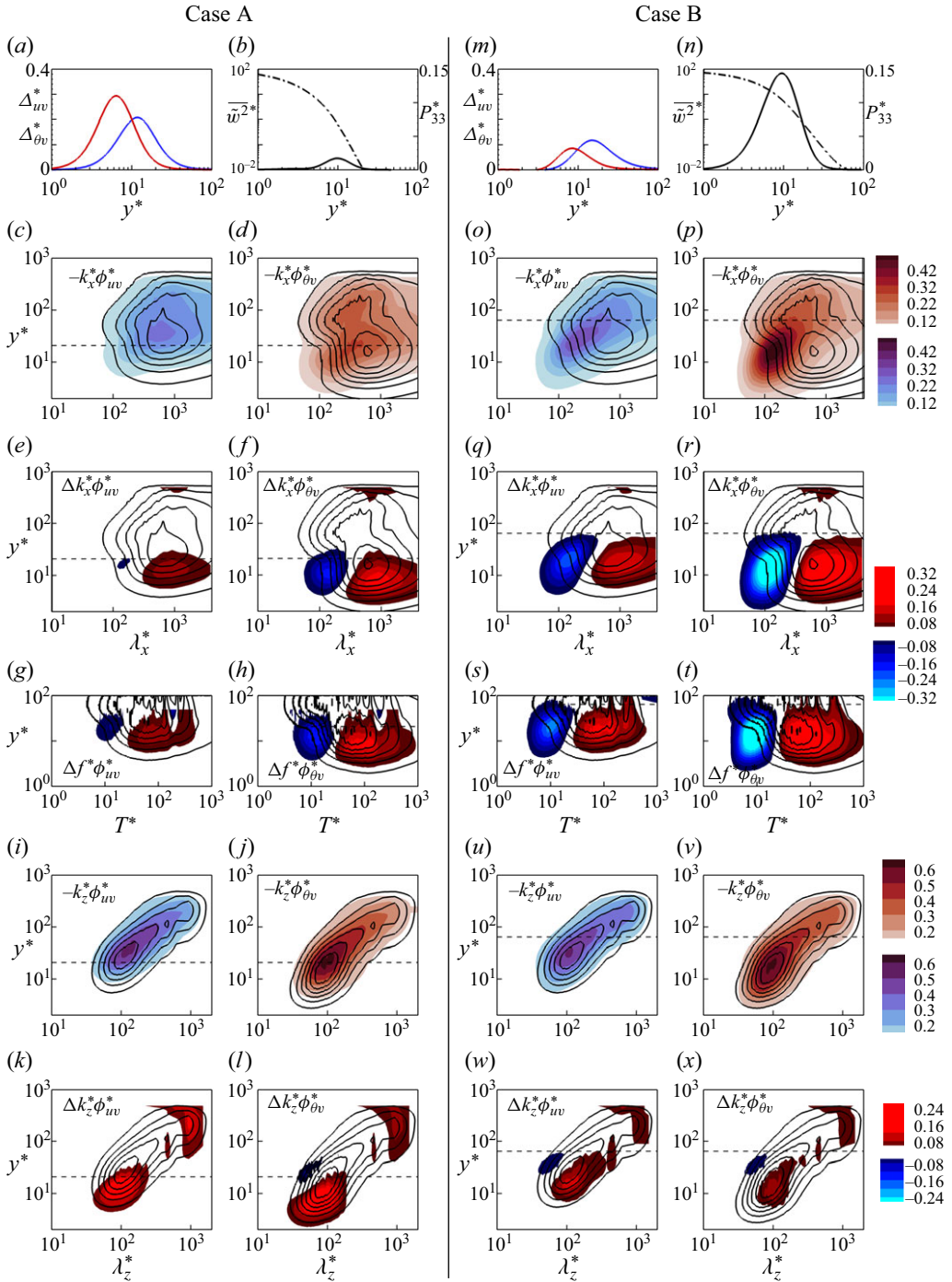


Figure 17. Comparisons between case A (left two columns) and case B (right two columns). (a,m) Profiles of Δ_{uv}^* (blue) and $\Delta_{\theta v}^*$ (red). (b,n) Profiles of \bar{w}^{2*} (dashed-dotted line) and P_{33}^* (solid line). Streamwise spectrograms: (c,o) $-k_x^*\phi_{uv}^*$; (d,p) $-k_x^*\phi_{\theta v}^*$ (contour lines and contour fields represent non-actuated and actuated cases, respectively). Difference between the actuated and non-actuated cases for the wavenumber spectra (e,f,q,r) and frequency spectra (g,h,s,t). Spanwise spectrograms: (i,u) $-k_z^*\phi_{uv}^*$; (j,v) $-k_z^*\phi_{\theta v}^*$. Difference between the actuated and non-actuated cases (k,l,w,x). In all the spectrograms, the horizontal dashed line marks $\ell_{0.01}^*$.

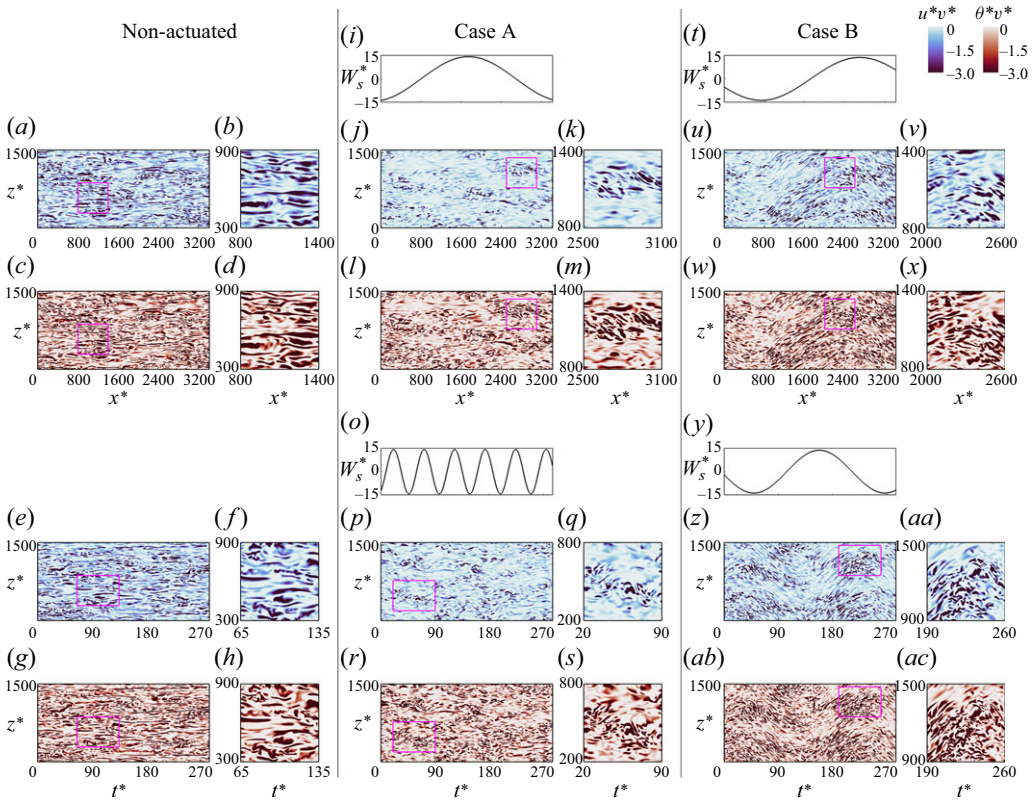


Figure 18. Visualisations of the instantaneous fields of u^*v^* (blue intensity fields) and θ^*v^* (brick intensity fields) at $y^+ = 14$ for the same cases as in figure 17. Next to each field, we magnify the small square outlined in pink. Left: non-actuated case; middle: actuated case A; right: actuated case B. The top two rows visualise u^*v^* and θ^*v^* at one time over the x^*-z^* plane. (i,t) Plot of the corresponding spanwise wall velocity W_s^* over x^* at the same time. The bottom two rows visualise u^*v^* and θ^*v^* at one x^* location over z^* and time t^* . (o,y) Plot of W_s^* over t^* at the same x^* location.

At a fixed ω^+ , u^*v^* and θ^*v^* are exposed to an identical Stokes layer. However, the larger change in $\Delta k_x^* \phi_{\theta v}^*$ compared with $\Delta k_x^* \phi_{uv}^*$ for $Pr > 1$ implies that the energetic near-wall scales of θ^*v^* are locally exposed to a stronger Stokes layer production. We establish this connection by evaluating the local Stokes layer production P_{33p}^* at the negative peaks of $\Delta k_x^* \phi_{\theta v}^*$ and $\Delta k_x^* \phi_{uv}^*$; these peaks are associated with the energetic small scales with $\lambda_x^* \simeq 10^2$ that contribute to the drop in I_{uv} and $I_{\theta v}$. Figure 19(b) demonstrates this process for case B (figure 17r), where the negative peak of $\Delta k_x^* \phi_{\theta v}^*$ is intersected with the P_{33}^* profile. With increasing Pr , the conductive sublayer thins and the negative peak in $\Delta k_x^* \phi_{\theta v}^*$ falls closer to the wall compared with its counterpart from $\Delta k_x^* \phi_{uv}^*$. This means that at each ω^+ , the energetic small scales of θ^*v^* are exposed to a larger Stokes layer production, and hence, have a higher energy. This leads to the drop in $I_{\theta v}$ compared with I_{uv} , as demonstrated in figure 19(a). At $Pr = 0.71$, the local production P_{33p}^* is close between u^*v^* and θ^*v^* , and I_{uv} and $I_{\theta v}$ are close to each other. However, at $Pr = 4.0$ and 7.5 , P_{33p}^* at each ω^+ is several times higher for θ^*v^* than u^*v^* , and $I_{\theta v}$ drops below I_{uv} . In addition, at $\omega^+ = 0.022$, P_{33p}^* increases by almost 3 times from $Pr = 0.71$ to 7.5 ,

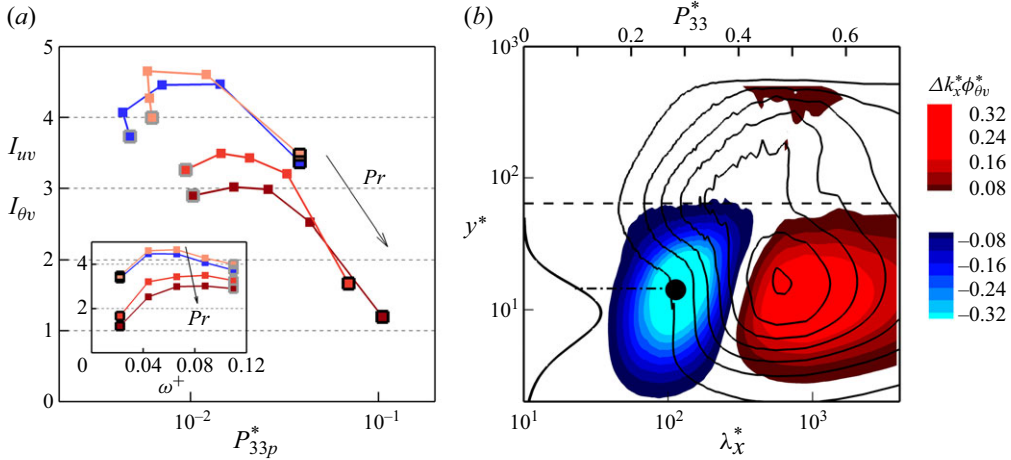


Figure 19. Assessment of the relation between I_{uv} and $I_{\theta v}$, and the local Stokes layer production P_{33p}^* at the negative peaks of $\Delta k_x^* \phi_{uv}^*$ and $\Delta k_x^* \phi_{\theta v}^*$. (a) Same data of I_{uv} and $I_{\theta v}$ as in figure 16(c), but versus P_{33p}^* ; to ease the inspection, the inset shows figure 16(c). The data points at $\omega^+ = 0.022$ and 0.110 have black and grey outlines, respectively. Panel (b) illustrates obtaining P_{33p}^* for case B (figure 17r), by intersecting the negative peak of $\Delta k_x^* \phi_{\theta v}^*$ with the P_{33}^* profile (on the left axis).

whereas at $\omega^+ = 0.110$, P_{33p}^* increases by 1.5 times. As a result, $I_{\theta v}$ has a milder decay rate at $\omega^+ = 0.110$ ($\gamma = 0.11$) than at $\omega^+ = 0.022$ ($\gamma = 0.53$).

We have seen how the behaviour of the Stokes layer leads to $I_{\theta v} < I_{uv}$ by examining the streamwise and frequency spectrograms. This connection is more difficult to find in the spanwise spectrograms $k_z^* \phi_{uv}^*$ and $k_z^* \phi_{\theta v}^*$ (figure 17i–l, $u-x$). The Stokes layer predominantly modifies the time scale T^* , hence, the streamwise length scale λ_x^* , of the near-wall turbulence. However, $k_z^* \phi_{uv}^*$ and $k_z^* \phi_{\theta v}^*$ are integrated over T^* and λ_x^* , and so the small-scale energy amplification is cancelled by the large-scale energy attenuation. Thus, even though the Stokes layer protrusion (production) increases from case A to case B, the distributions of $k_z^* \phi_{uv}^*$ and $k_z^* \phi_{\theta v}^*$ suggest that the near-wall turbulence is distorted to a lesser extent.

Our observations regarding the large-scale attenuation and small-scale amplification can be extended by applying scale-wise decomposition to Δ_{uv}^* and $\Delta_{\theta v}^*$. For instance, we can write $\Delta_{uv}^* = \Delta_{uv+}^* + \Delta_{uv-}^*$, where

$$\Delta_{uv+}^* = \int_{\lambda_x^* > 350} \Delta \phi_{uv}^*(k_x^*, y^*) dk_x^* - y^* (Re_{\tau}^{-1} - Re_{\tau_0}^{-1}), \quad (3.9a)$$

$$\Delta_{uv-}^* = \int_{\lambda_x^* \leq 350} \Delta \phi_{uv}^*(k_x^*, y^*) dk_x^*. \quad (3.9b)$$

We set the threshold of $\lambda_x^* = 350$ for partitioning because the spectrograms for all cases show $\Delta k_x^* \phi_{uv}^* > 0$ for $\lambda_x^* \gtrsim 350$ and $\Delta k_x^* \phi_{uv}^* < 0$ for $\lambda_x^* \lesssim 350$ (see figure 17e,q). As noted earlier (figure 10a and (3.3a)), we need to subtract the term $y^*(Re_{\tau}^{-1} - Re_{\tau_0}^{-1})$ from $\Delta \bar{u}\bar{v}^*$ to obtain its net contribution Δ_{uv}^* . Considering figure 17(e,q), this contribution appears in the large scales of $\Delta k_x^* \phi_{uv}^*$ ($\lambda_x^* > 350$), and therefore, we subtract $y^*(Re_{\tau}^{-1} - Re_{\tau_0}^{-1})$ from the large-scale integration (3.9a). The same reasoning is applied to the partitioning of $\Delta_{\theta v}^*$, and we calculate $\Delta_{\theta v+}^*$ and $\Delta_{\theta v-}^*$ in a manner that is identical to that expressed by (3.9a) and (3.9b).

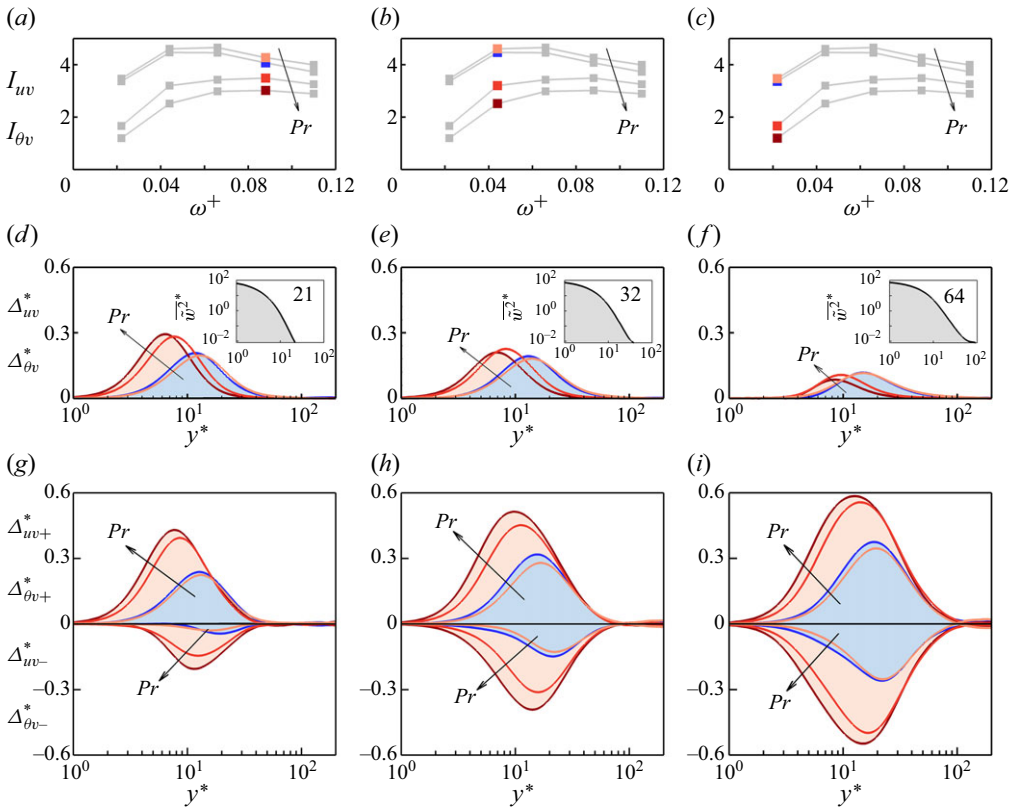


Figure 20. Large- and small-scale contributions to Δ_{uv}^* , $\Delta_{\theta v}^*$ and their integrals I_{uv} , $I_{\theta v}$ for the travelling wave case. Left column: $\omega^+ = 0.088$; middlecolumn: $\omega^+ = 0.044$; rightcolumn: $\omega^+ = 0.022$. Blue uv profiles; for θv profiles, $Pr = 0.71$ is shown in light orange, $Pr = 4.0$ in orange and $Pr = 7.5$ in brick red. (a,b,c) Plot of I_{uv} , $I_{\theta v}$ versus ω^+ . (d,e,f) Plot of Δ_{uv}^* , $\Delta_{\theta v}^*$ versus y^* ; the insets plot \overline{w}^{2*} representing the Stokes layer where the number reports $\ell_{0,01}^*$. (d,e,f) Total Δ_{uv}^* , $\Delta_{\theta v}^*$; (g,h,i) decomposed $\Delta_{uv\pm}^*$, $\Delta_{\theta v\pm}^*$. In (d–i) we shade under the profiles of Δ_{uv}^* and $\Delta_{\theta v}^*$ at $Pr = 7.5$, as well as their decomposition.

Figure 20 shows how changing ω^+ or Pr modifies the balance between the large-scale attenuation (Δ_{uv+}^* , $\Delta_{\theta v+}^*$) and the small-scale amplification (Δ_{uv-}^* , $\Delta_{\theta v-}^*$). The net attenuations Δ_{uv}^* and $\Delta_{\theta v}^*$ (figure 20d,e,f) depend on the disparity between their decomposed parts (figure 20g,h,i). Decreasing ω^+ (increasing the Stokes layer protrusion) simultaneously increase Δ_{uv+}^* , $\Delta_{\theta v+}^*$ and Δ_{uv-}^* , $\Delta_{\theta v-}^*$. However, below the optimal ω^+ , $\Delta_{\theta v-}^*$, Δ_{uv-}^* increase more than $\Delta_{\theta v+}^*$, Δ_{uv+}^* , leading to the drop in I_{uv} , $I_{\theta v}$. We demonstrate this by shading the areas under $\Delta_{\theta v}^*$ and its decompositions at $Pr = 7.5$ light orange. From the optimal $\omega^+ = 0.088$ (figure 20g) to 0.022 (figure 20i), $\Delta_{\theta v-}^*$ increases more than $\Delta_{\theta v+}^*$, and $I_{\theta v}$ decreases. At each ω^+ , increasing Pr increases $\Delta_{\theta v-}^*$ more than $\Delta_{\theta v+}^*$, hence, the drop in $I_{\theta v}$. This is due to the thinning of the conductive sublayer and the increase in the local Stokes layer production, as discussed with respect to figure 19.

3.8. Comparison between the travelling wave and the plane oscillation

All our findings based on the travelling wave motion (§§ 3.3–3.7) remain broadly valid for the case of plane oscillation. By comparing figures 21 and 22 with figures 13 and 16, we see that, for example, the power-law relation $I_{\theta v} = I_{uv}/Pr^\gamma$ fits well with the plane oscillation data (figure 21a), and the division $HR > DR$ ($\gamma < 0.5$) and $HR < DR$ ($\gamma > 0.5$) is also

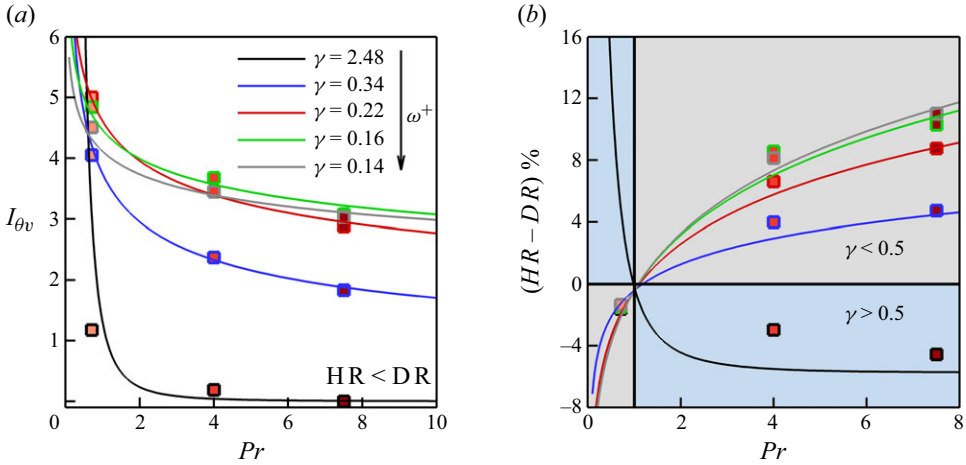


Figure 21. Similar plots as in figure 13(b,d), but for the plane oscillation with $A^+ = 12$ (figure 3c). The outline colour of each data point indicates its ω^+ ; $\omega^+ = 0.022$ (black), 0.044 (blue), 0.066 (red), 0.088 (green) and 0.110 (grey).

valid (figure 21b). The value of γ at each ω^+ is close to its counterpart for the travelling wave case, with the exception of $\omega^+ = 0.022$, where $\gamma = 2.48$ for the plane oscillation (black lines in figure 21), almost five times larger than the value of 0.53 found for the travelling wave motion. Such a strong decay rate drops $I_{\theta v}$ to almost zero by $Pr = 7.5$ for the plane oscillation, leading to $HR - DR \simeq -5\%$. This strong decay is associated with the appearance of a highly protrusive Stokes layer (figure 22a,c), in agreement with the discussion given in § 3.7.

Figure 22 shows that, for $0.066 \leq \omega^+ \leq 0.110$, DR, HR, I_{uv} , $I_{\theta v}$ and $\ell_{0.01}^*$ for the plane oscillation are close to the values found for the travelling wave. However, as ω^+ decreases to 0.044 and then to 0.022, significant differences appear. For the plane oscillation, the Stokes layer becomes highly protrusive, reaching up to $\ell_{0.01}^* \simeq 120$ at $\omega^+ = 0.022$. As discussed in § 3.7, such a protrusive Stokes layer loses its efficacy in producing a net attenuation of the near-wall turbulence. As a result, I_{uv} and $I_{\theta v}$ significantly drop and γ rises significantly. Rouhi *et al.* (2023) showed that when $\ell_{0.01}^* \sim \mathcal{O}(10^2)$, the Stokes layer departs from its laminar-like structure, the mean velocity and temperature profiles become highly disturbed (figure 28j,k,l), and the predictive relations for DR (3.5a) and HR (3.5b) begin to fail. Similarly, we observe that at $\omega^+ = 0.022$ the predictive relation for HR (3.5b) is much less accurate compared with its performance at higher frequencies (figure 21b).

As a final note, it appears that γ , a Pr -independent quantity, increases almost linearly with $\ell_{0.01}^*$ and $P_{33,max}^*$, and decreases inversely with increasing ω^+ following

$$\gamma \simeq 4.2 P_{33,max}^* \simeq 0.008 \ell_{0.01}^* \simeq 1/(80\omega^+). \tag{3.10}$$

This is supported by the results shown in figure 23, where we compile all our data for the travelling wave and the plane oscillation cases (with the exception of the plane oscillation at $\omega^+ = 0.022$ where the Stokes layer is particularly protrusive). Our present data are at a fixed $A^+ = 12$ for a plane oscillation ($\kappa_x^+ = 0$) and a travelling wave ($\kappa_x^+ = 0.0014$). The relation for γ (3.10) is expected to also depend on A^+ and κ_x^+ . However, for the upstream travelling wave with $\omega^+ \gtrsim 0.04$, we anticipate γ to weakly depend on κ_x^+ . Our conjecture is partly based on the validity of (3.10) for $\kappa_x^+ = 0$ and $\kappa_x^+ = 0.0014$ for $\omega^+ \gtrsim 0.04$. Furthermore, γ relates $\Delta \overline{\Theta}_{170}^*$ to $\Delta \overline{U}_{170}^*$, which $\Delta \overline{U}_{170}^*$ is seen to weakly depend

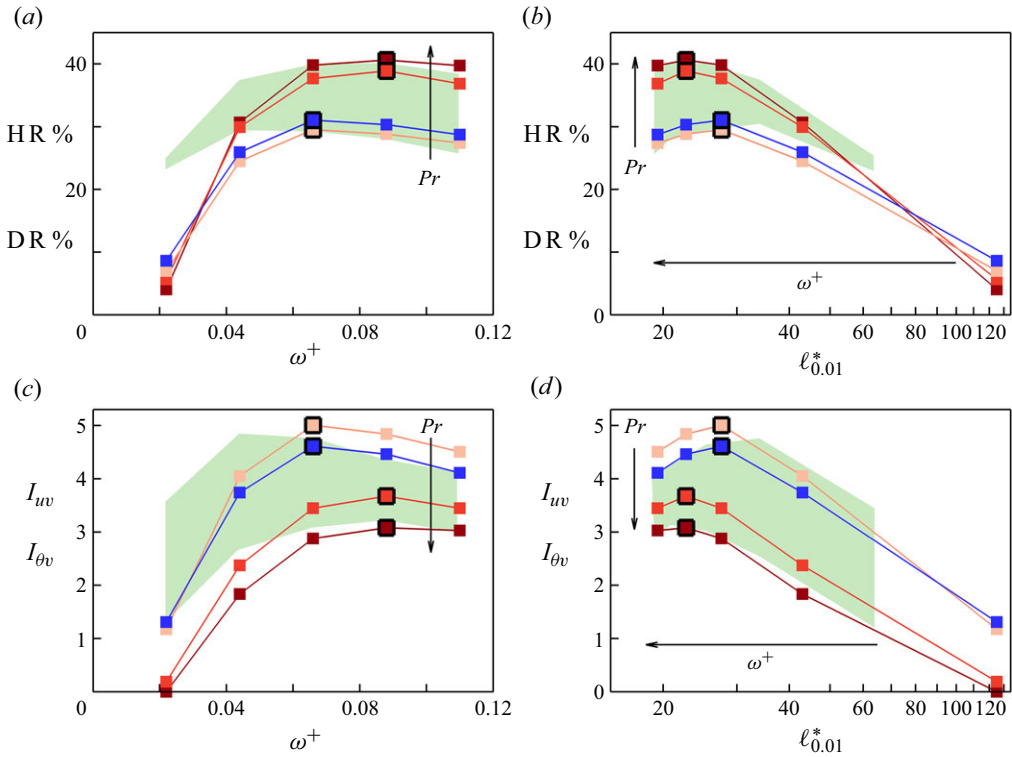


Figure 22. Same plots as in figure 16, except the data points (filled squares) are from the plane oscillation with $A^+ = 12$. The range of variations in the travelling wave data points are shaded in green.

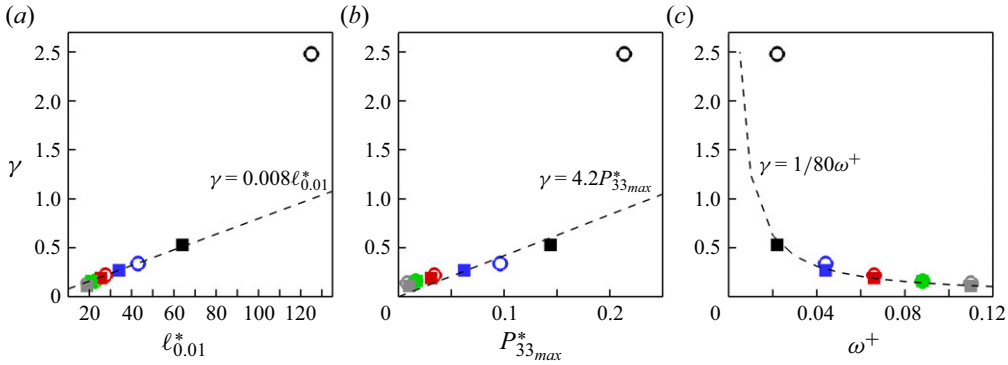


Figure 23. Assessment of the relations (3.10) between γ , P_{33max}^* , $\ell_{0.01}^*$ and ω^+ for the travelling wave (filled squares) and the plane oscillation (empty circles); $\omega^+ = 0.022$ (black), 0.044 (blue), 0.066 (red), 0.088 (green) and 0.110 (grey).

on κ_x^+ for the upstream travelling wave with $\omega^+ \gtrsim 0.04$ (see figure 13 in Gatti & Quadrio 2016), and we anticipate $\Delta\bar{\Theta}_{170}^*$ to behave similarly.

4. Conclusions

Direct numerical simulations of turbulent half-channel flow with forced convection were performed at a friction Reynolds number of 590 for Prandtl numbers of 0.71 (air), 4.0,

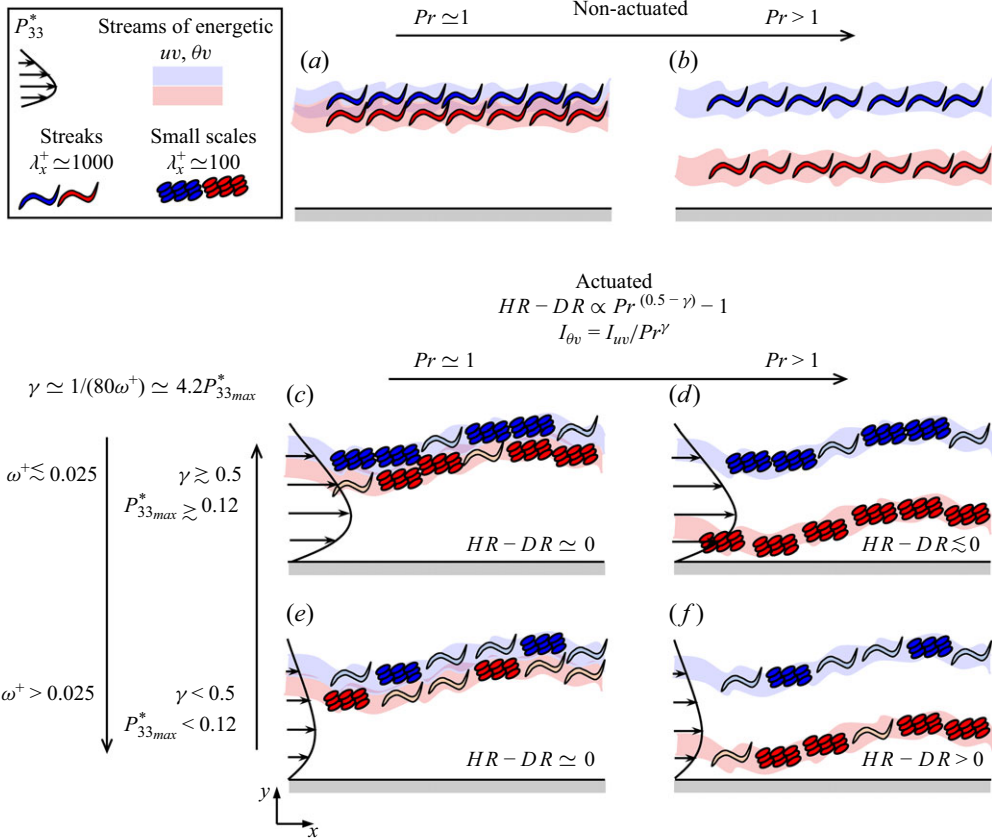


Figure 24. Schematic illustration of our findings from §§ 3.4 to 3.8. The meaning of each sketch is written in the top-left framed area. (a–f) Near-wall illustration of the energetic scales of uv and θv for (a,b) non-actuated cases and (c–f) actuated cases. Panels (a,c,e) correspond to $Pr \simeq 1$, and (b,d,f) correspond to $Pr > 1$. For the actuated cases, (c,d) represent $\omega^+ \lesssim 0.025$ and (e,f) represent $\omega^+ > 0.025$. The Stokes layer production profile is drawn for each actuated case.

7.5 (water) and 20 (molten salt). Spanwise wall forcing was applied either as a plane wall oscillation or a streamwise in-plane travelling wave with wavenumber $\kappa_x^+ = 0.0014$ ($\lambda_x^+ \simeq 4500$). For both oscillation mechanisms, we fix the amplitude $A^+ = 12$ and change the frequency from $\omega^+ = 0.022$ to 0.110 (upstream travelling waves only).

The key finding of the present work is that, for $\omega^+ > 0.022$ and $Pr > 1$, we achieve $HR > DR$; especially, for $\omega^+ \gtrsim 0.066$ and $Pr \gtrsim 4.0$, there is a significant disparity between $HR \simeq 40\%$ and $DR \simeq 30\%$. On the other hand, for $\omega^+ \leq 0.022$ and $Pr > 1$, $HR \lesssim DR$. These results apply to the travelling wave motion and the plane oscillation. To help understand these results, we derived explicit relations between HR and DR and the integrals of the attenuation in the turbulent shear stress (I_{uv}) and turbulent temperature flux ($I_{\theta v}$). Figure 24 summarises how I_{uv} and $I_{\theta v}$ change with Pr and ω^+ , and illustrates the underlying physics. For the cases considered here, we find that $I_{\theta v} \simeq I_{uv} / Pr^\gamma$, where $\gamma \simeq 1 / (80\omega^+) \simeq 4.2P_{33}^*_{max}$ is proportional to the Stokes layer production P_{33}^* . Therefore, we expect $I_{\theta v}$ to fall below I_{uv} for $Pr > 1$ and for increasing γ (decreasing ω^+ and increasing P_{33}^*). Stokes layer production attenuates the energy of the streak-like scales with $\lambda_x^+ \simeq 1000$ (hence, the rise in I_{uv} , $I_{\theta v}$), but generates small scales with $\lambda_x^+ \simeq 100$ and amplifies their energy (hence, the drop in I_{uv} , $I_{\theta v}$). At a fixed ω^+ (γ), increasing

Pr towards $Pr > 1$, thins the conductive sublayer, and the energetic small scales of θv travel closer to the wall, and locally are exposed to a larger Stokes layer production compared with those of uv . Larger Stokes layer production means larger amplification of energy in the small scales of θv compared with uv , leading to $I_{\theta v} < I_{uv}$ (figure 24*d,f*). In other words, for $Pr > 1$, the energy attenuation of θv is less than uv . Nevertheless, by exploiting $I_{\theta v} \simeq I_{uv}/Pr^\gamma$, we arrive at $HR - DR \propto Pr^{(0.5-\gamma)} - 1$, as HR depends on $\Delta\bar{\Theta}^* = Pr I_{\theta v} = Pr^{(1-\gamma)} I_{uv}$, and the non-actuated Stanton number that decays with Pr . Therefore, we can achieve $HR - DR > 0$ if $\gamma \lesssim 0.5$ ($\omega^+ \gtrsim 0.025$). These findings and the relations between $HR - DR$, ω^+ , γ and P_{33max}^* agree well with our DNS data for both the travelling wave and the plane oscillation.

The time scale of the near-wall energetic temperature scales \mathcal{T}_θ^+ was found to be almost insensitive to Pr , and it remains close to its counterpart for the velocity scales $\mathcal{T}_u^+ \simeq 100$. As a result, for the plane oscillation, the optimal value of ω^+ for the maximum HR is close to that for the maximum DR, that is, $\omega^+ \simeq 2\pi/100 \simeq 0.066$. However, for the travelling wave, the optimal frequency for HR changes from 0.044 at $Pr = 0.71$ to 0.088 at $Pr = 7.5$ because it depends on the advection speed of the energetic temperature scales. The thinning of the conductive sublayer decreases the advection speed, and so the optimal frequency of actuation increases.

From the Prandtl number scaling of the thermal statistics, we derived a predictive model for HR. By knowing γ and I_{uv} for a fixed set of actuation parameters (A^+ , κ_x^+ , ω^+) at a given Reynolds and Prandtl number, the model predicts HR at other Prandtl and Reynolds numbers. Using this model, we generated a map $HR(Pr, Re_{\tau_0})$ for the optimal case with $\omega^+ = 0.088$, and found good agreement with the computations for Prandtl numbers up to 7.5. To further evaluate the model, we conducted an extra simulation at $\omega^+ = 0.088$ and $Pr = 20$, $Re_{\tau_0} = 590$. Again, good agreement with the model was found (DNS HR = 43 %, HR - DR = 13 % compared with the model HR = 45 %, HR - DR = 14 %).

As an early systematic work on turbulent heat-transfer control by spanwise wall forcing, we focused on Pr and $\omega^+ > 0$, due to their significant effect on HR and HR - DR. Our findings are encouraging to pursue this work towards investigating the effects of A^+ , κ_x^+ , Re_{τ_0} and $\omega^+ < 0$ (downstream travelling wave). We anticipate that our discoveries could be applied to a wider parameter space. Our conjecture is partly supported by the validity of our findings for both the travelling wave and plane oscillation in the present study. Also, similar findings for DR are shown to be applicable to a wide parameter space of (A^+ , ω^+ , κ_x^+ , Re_{τ_0}). The prediction model for DR by Gatti & Quadrio (2016), the analogue of our model for HR, is shown to agree well with the DNS (Gatti *et al.* 2024) and LES (Rouhi *et al.* 2023) data for $1000 \lesssim Re_{\tau_0} \lesssim 6000$ over the actuation parameter space where DR significantly changes ($5 \leq A^+ \leq 12$, $0 \leq \kappa_x^+ \leq 0.02$, $-0.2 \leq \omega^+ \leq 0.2$). Also, the findings related to the Stokes layer protrusion and DR are found to be valid over the range of κ_x^+ considered so far. For instance, up to the Stokes layer thickness $\delta_S^* \simeq 6$ (protrusion height $\ell_{0,01}^* \simeq 25$), there is a linear relation between DR, $\ell_{0,01}^*$ and δ_S^* , regardless of the value of κ_x^+ (Quadrio & Ricco 2011; Rouhi *et al.* 2023). This is because the modification of the velocity scales by the Stokes layer is similar between the plane oscillation (Touber & Leschziner 2012) and the travelling wave at different values of κ_x^+ (Rouhi *et al.* 2023).

Acknowledgements. We acknowledge Dr Daniel Chung for providing his DNS solver. We thank EPSRC for the computational time made available on ARCHER2 via the UK Turbulence Consortium (EP/R029326/1), and the UKRI access to the HPC call 2024. We also acknowledge Intellectual Ventures for providing additional computational time on ARCHER2.

Funding. The research was funded through the Deep Science Fund of Intellectual Ventures.

Set-up	Re_{τ_0}	Pr	L_x, L_z	Δ_x^+, Δ_z^+	Δ_y^+	C_{f_0}	Nu_0	Legend
Full fine	590	7.5	$2\pi h, \pi h$	3.6, 1.8	0.12 – 3.8	0.0058	162	—
Reduced coarse	590	7.5	$2.7h, 0.85h$	8.3, 3.9	0.28 – 8.5	0.0057	162	---
MKM99	590	—	$2\pi h, \pi h$	9.7, 4.8	0.09 – 7.2	0.0057	—	■
AH21	500	7.0	$2\pi h, \pi h$	8.2, 4.1	0.27 – 3.9	—	132	○

Table 2. Validation simulations for the reduced coarse set-up. Non-actuated half-channel flow at $Pr = 7.5$. Statistics for these cases are shown in figure 25. The reference cases are MKM99 (Moser *et al.* 1999) and AH21 (Alcántara-Ávila & Hoyas 2021).

Declaration of interests. The authors report no conflict of interest.

Appendix A. Validation of the grid and the domain size

The production runs were performed in a reduced-domain half-channel flow ($L_x \gtrsim 2.7h, L_z \simeq 0.85h$) with grid resolution $\Delta_x^+ \times \Delta_z^+ \simeq 8 \times 4$; we call this set-up ‘reduced coarse’. To check that this set-up gives accurate DR, HR and statistics of interest over our parameter space, calculations with a finer grid resolution of $\Delta_x^+ \times \Delta_z^+ \simeq 4 \times 2$ were conducted in a full domain ($L_x \gtrsim 2\pi h, L_z \simeq \pi h$); we call this set-up ‘full fine’. Two additional set-ups were also used, called ‘full coarse’ ($L_x \gtrsim 7.6h, L_z \simeq \pi h, \Delta_x^+ \times \Delta_z^+ \simeq 8 \times 4$) and ‘full intermediate’ ($L_x \gtrsim 7.6h, L_z \simeq \pi h, \Delta_x^+ \times \Delta_z^+ \simeq 6 \times 3$). For all simulations, $Re_{\tau_0} = 590$ and $A^+ = 12$. For all the reduced-domain cases, we reconstruct the \bar{U}^* and $\bar{\Theta}^*$ profiles beyond $y_{res}^* = 170$, and calculate DR and HR following our approach in § 2.3.

For the non-actuated half-channel flow at $Pr = 7.5$, table 2 shows that for the full fine and reduced coarse set-ups, the Nusselt numbers Nu_0 are identical and the skin-friction coefficients C_{f_0} differ by less than 2%. The profiles of $\bar{U}^+, \bar{\Theta}^+$, turbulent stresses $\overline{u^2}^+, \overline{v^2}^+, \overline{w^2}^+$ and mean square of turbulent temperature $\overline{\theta^2}^+$ are also in excellent agreement (figure 25). Compared with the reference data, our obtained C_{f_0} from the reduced coarse case is identical to that from Moser *et al.* (1999) (table 2); similarly, our velocity statistics up to $y_{res}^+ \simeq 200$ are in excellent agreement (figure 25). In terms of the temperature statistics $\bar{\Theta}^+, \overline{\theta^2}^+$, the small differences between our results and those from Alcántara-Ávila & Hoyas (2021) are most likely due to the differences in Re_{τ_0} and Pr (590 compared with 500 and 7.5 compared with 7).

For the actuated half-channel flow cases at $Pr = 0.71$ and 7.5, table 3 lists three sets of validation cases. For set 1, we compare the ‘reduced coarse’ set-up with the ‘full coarse’ set-up because the grid resolution of $\Delta_x^+ \times \Delta_z^+ \simeq 8 \times 4$ is fine enough at this Pr (Pirozzoli *et al.* 2016; Alcántara-Ávila *et al.* 2018, 2021; Alcántara-Ávila & Hoyas 2021). Sets 1 and 2 are travelling wave cases, and set 3 is for the plane oscillation case. For each set, we see that reducing the domain size and coarsening the grid from the full fine set-up to the reduced coarse set-up changes DR and HR by a maximum of 1.5% and 1.9%, respectively.

Set 2 contains the most challenging cases over the range $0.71 \leq Pr \leq 7.5$ in terms of their grid resolution requirement. In figure 26 we compare the mean velocity \bar{U}^* and the mean temperature $\bar{\Theta}^*$ profiles for $Pr = 7.5$. In terms of the \bar{U}^* profiles, the reduced coarse set-up is almost identical to the full fine set-up up to $y_{res}^* \simeq 170$. Beyond y_{res}^* , the reconstructed \bar{U}^* profiles for the reduced coarse set-up agree well with the full fine set-up. In terms of the $\bar{\Theta}^*$ profiles, excellent agreement is obtained between the full fine set-up and the reduced coarse set-up at $\omega^+ = 0.022$ and 0.088 (figure 26a,c). At $\omega^+ = 0.044$,

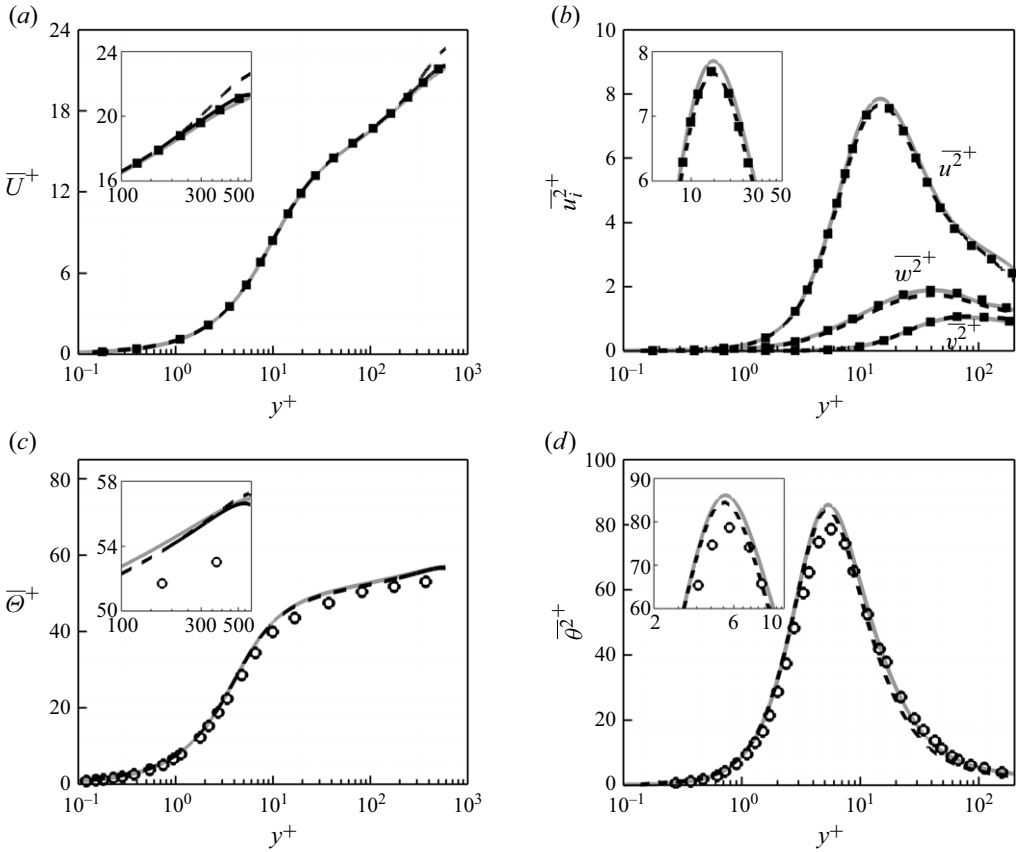


Figure 25. Comparing the results for the three set-ups given in table 2. (a) Mean velocity profiles \bar{U}^+ . (b) Turbulent stresses $\overline{u^2}^+$, $\overline{v^2}^+$, $\overline{w^2}^+$. (c) Mean temperature profiles $\bar{\Theta}^+$. (d) Mean square of turbulent temperature $\overline{\theta^2}^+$. Solid grey line, ‘full fine’ set-up. Dashed line: ‘reduced coarse’ set-up. The solid black line in (a,c) is the reconstructed profile for $y^+ \geq 200$, as in § 2.3. Square symbols: DNS of Moser *et al.* (1999). Circle symbols: DNS of Alcántara-Ávila & Hoyas (2021).

there is some sensitivity to the grid, where at $y^* = 200$, $\bar{\Theta}^* = 74.3$ for the full fine set-up and 73.0 for the reduced coarse set-up. This difference (1.3 units) is small relative to the temperature difference $\Delta \bar{\Theta}_{200}^* \simeq 19.0$ between the actuated and non-actuated profiles. In figure 27 we assess the accuracy of the reduced coarse set-up in resolving $\overline{u^2}^*$ and $\overline{\theta^2}^*$, as well as their pre-multiplied spectrograms $k_x^* \phi_{uu}^*$, $k_z^* \phi_{uu}^*$, $k_x^* \phi_{\theta\theta}^*$, $k_z^* \phi_{\theta\theta}^*$ at $\omega^+ = 0.044$. The reduced coarse set-up results agree well with the full fine set-up results, especially in matching the energetic peaks in the spectrograms in terms of magnitude, location y^* and length scales λ_x^* , λ_z^* .

Table 4 summarises our validation study at $Pr = 20.0$ (table 1). For the non-actuated case (table 4), C_{f_0} and C_{h_0} from the coarse grid results differ from the intermediate grid results by a maximum of 0.5 %, and for the travelling wave case, DR and HR differ by < 1 %.

Based on these results, we conclude that DR, HR and the statistics of interest can be accurately computed using the reduced coarse set-up with the grid resolution of $\Delta_x^+ \times \Delta_z^+ \simeq 8 \times 4$, and the domain size of $L_x \times L_z \simeq 7.6h \times 0.85h$ for the travelling wave case ($\kappa_x^+ = 0.0014$), and the domain size of $L_x \times L_z \simeq 2.7h \times 0.85h$ for the plane oscillation

Case	ω^+	L_x, L_z	Δ_x^+, Δ_z^+	Δ_y^+	DR %	HR %		
Full coarse	0.022	$7.6h, \pi h$	7.4, 3.9	0.20 – 6.0	24.5	23.3	Set 1 $Pr = 0.71$ $\kappa_x^+ = 0.0014$	
Reduc. coarse	0.022	$7.6h, 0.85h$	8.8, 3.9	0.28 – 8.5	25.2	23.6		
Full coarse	0.044	$7.6h, \pi h$	7.4, 3.9	0.20 – 6.0	30.4	29.1	$\epsilon_{DRmax}, \epsilon_{HRmax}$ 0.7 %, 0.6 %	
Reduc. coarse	0.044	$7.6h, 0.85h$	8.8, 3.9	0.28 – 8.5	30.6	29.3		
Full coarse	0.088	$7.6h, \pi h$	7.4, 3.9	0.20 – 6.0	29.9	28.5		
Reduc. coarse	0.088	$7.6h, 0.85h$	8.8, 3.9	0.28 – 8.5	29.3	27.9		
							Line	
Full fine	0.022	$7.6h, \pi h$	3.9, 1.8	0.12 – 3.8	26.2	25.4	—	Set 2 $Pr = 7.5$ $\kappa_x^+ = 0.0014$
Reduc. coarse	0.022	$7.6h, 0.85h$	8.8, 3.9	0.28 – 8.5	25.6	24.0	---	
Full fine	0.044	$7.6h, \pi h$	3.9, 1.8	0.12 – 3.8	31.4	38.6	—	$\epsilon_{DRmax}, \epsilon_{HRmax}$ 1.5 %, 1.6 %
Full inter.	0.044	$7.6h, \pi h$	5.8, 2.7	0.18 – 5.7	30.9	37.7	---	
Full coarse	0.044	$7.6h, \pi h$	8.8, 4.0	0.28 – 8.5	31.0	37.0	
Reduc. coarse	0.044	$7.6h, 0.85h$	8.8, 3.9	0.28 – 8.5	31.8	37.7	---	
Full fine	0.088	$7.6h, \pi h$	3.9, 1.8	0.12 – 3.8	29.0	39.8	—	Set 3 $Pr = 7.5$ $\kappa_x^+ = 0$
Reduc. coarse	0.088	$7.6h, 0.85h$	8.8, 3.9	0.28 – 8.5	30.5	40.4	---	
Full fine	0.044	$2\pi h, \pi h$	3.6, 1.8	0.12 – 3.8	25.2	28.9		$\epsilon_{DRmax}, \epsilon_{HRmax}$ 1.4 %, 1.9 %
Reduc. coarse	0.044	$2.7h, 0.85h$	8.3, 3.9	0.28 – 8.5	26.5	30.8		
Full fine	0.088	$2\pi h, \pi h$	3.6, 1.8	0.12 – 3.8	29.4	39.0		
Reduc. coarse	0.088	$2.7h, 0.85h$	8.3, 3.9	0.28 – 8.5	30.8	40.7		

Table 3. Validation simulations for grid and domain size.

case ($\kappa_x^+ = 0$). These grid and domain size prescriptions were used for our production calculations (table 1).

Appendix B. Relation between HR and temperature difference

The mean velocity \bar{U}^* and temperature $\bar{\Theta}^*$ profiles in the log region and beyond can be expressed based on the following semi-empirical wall-wake relations (Rouhi *et al.* 2022):

$$\bar{U}^* = \frac{1}{\kappa_u} \ln(y^*) + B_u + \frac{2\Pi_u}{\kappa_u} \mathcal{W}_u(y/h) + \Delta\bar{U}_{log}^*, \quad (C1a)$$

$$\bar{\Theta}^* = \frac{1}{\kappa_\theta} \ln(y^*) + B_\theta + \frac{2\Pi_\theta}{\kappa_\theta} \mathcal{W}_\theta(y/h) + \Delta\bar{\Theta}_{log}^*. \quad (C1b)$$

Here κ_u, κ_θ and B_u are constants, but the offset B_θ depends on Pr (Kader & Yaglom 1972; Kader 1981). The wake profiles $(2\Pi_u/\kappa_u)\mathcal{W}_u(y/h)$ and $(2\Pi_\theta/\kappa_\theta)\mathcal{W}_\theta(y/h)$ depend on the flow configuration, e.g. channel, pipe or boundary layer (Pope 2000; Nagib & Chauhan 2008). The log-law shifts, $\Delta\bar{U}_{log}^*$ and $\Delta\bar{\Theta}_{log}^*$, are non-zero for the actuated cases. These log-law shifts are evaluated at $y^* = 170$, where $\Delta\bar{U}^*$ and $\Delta\bar{\Theta}^*$ approximately reach their asymptotic values (figures 4 and 8). For fixed operating parameters ($A^+, \kappa_x^+, \omega^+$), $\Delta\bar{U}_{log}^*$ is constant for the upstream travelling wave (Hurst *et al.* 2014; Gatti & Quadrio 2016; Rouhi *et al.* 2023). However, $\Delta\bar{\Theta}_{log}^*$ strongly depends on Pr (figure 8k,l). We set the constants $\kappa_u = 0.4, \kappa_\theta = 0.46$ and $B_u = 5.2$ following Pirozzoli *et al.* (2016) and Rouhi *et al.* (2022),

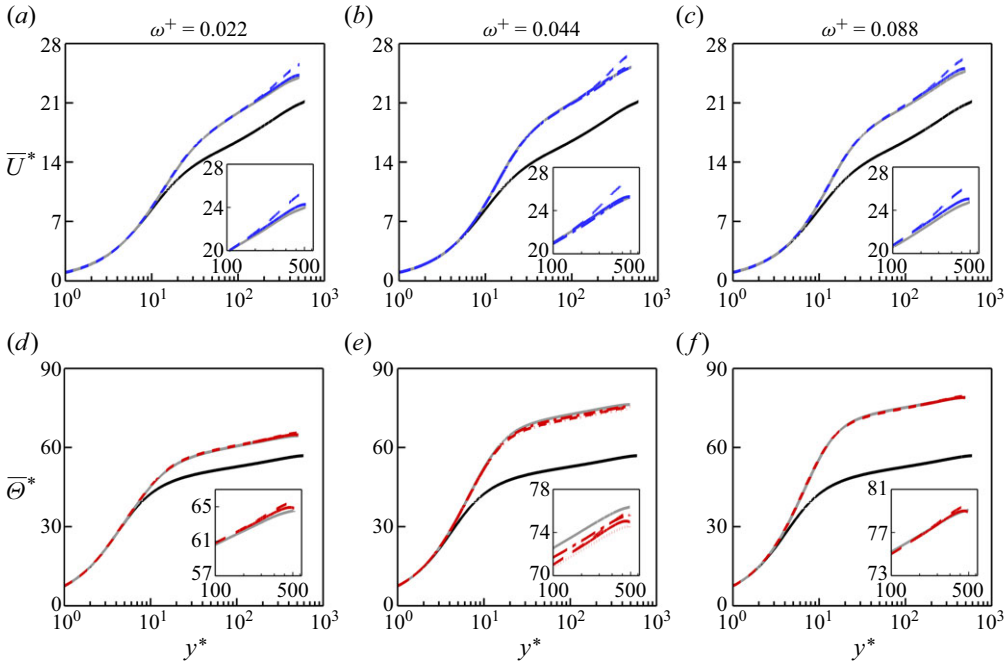


Figure 26. Comparison of the mean velocity (*a,b,c*) and the mean temperature (*d,e,f*) profiles for the travelling wave at $Pr = 7.5$ (set 2, table 3). Results are shown for (*a,d*) $\omega^+ = 0.022$, (*b,e*) $\omega^+ = 0.044$ and (*c,f*) $\omega^+ = 0.088$. Solid grey line: ‘full fine’ case. Dashed-dotted line: ‘full inter.’ case. Dotted line: full coarse case. Dashed line: ‘reduc. coarse’ case. Solid blue and red lines are the reconstructed profiles for $y^* \geq 170$, as in § 2.3. Solid black line: non-actuated ‘full fine’ case.

and obtain the offset $B_\theta(Pr) = 12.5Pr^{2/3} + 2.12 \ln Pr - 5.3$ following Kader & Yaglom (1972), which is reported to be accurate for $Pr \gtrsim 0.7$. The suitability of these choices is confirmed in § 2.3 and Appendix A.

The bulk velocity U_b^* and bulk temperature Θ_b^* are found by integrating (C1a) and (C1b), so that

$$U_b^* = \frac{1}{\kappa_u} \ln(Re_\tau) - \frac{1}{\kappa_u} + B_u + \frac{2\Pi_u}{\kappa_u} \int_0^h \mathcal{W}_u(y/h) dy + \Delta \bar{U}_{log}^*, \quad (C2a)$$

$$\Theta_b^* = \frac{1}{\kappa_\theta} \ln(Re_\tau) - \frac{1}{\kappa_\theta} + B_\theta + \frac{2\Pi_\theta}{\kappa_\theta} \int_0^h \mathcal{W}_\theta(y/h) dy + \Delta \bar{\Theta}_{log}^*. \quad (C2b)$$

By subtracting the non-actuated $U_{b_0}^*$ and $\Theta_{b_0}^*$ from their actuated counterparts U_b^* and Θ_b^* , and by assuming that the wake profiles are not influenced by the wall oscillation, we obtain

$$U_b^* - U_{b_0}^* = \frac{1}{\kappa_u} \ln \left(\frac{Re_\tau}{Re_{\tau_0}} \right) + \Delta \bar{U}_{log}^*, \quad \Theta_b^* - \Theta_{b_0}^* = \frac{1}{\kappa_\theta} \ln \left(\frac{Re_\tau}{Re_{\tau_0}} \right) + \Delta \bar{\Theta}_{log}^*. \quad (C3a,b)$$

When Re_τ is matched between the actuated and non-actuated cases ($Re_\tau = Re_{\tau_0}$), the first term on the right-hand side of (C3) disappears. However, when the bulk Reynolds number Re_b is matched, as in our work, this term is retained because $Re_\tau \neq Re_{\tau_0}$. By using (C3) and the relations $C_f = 2/U_b^{*2}$, $C_h = 1/(U_b^* \Theta_b^*)$, $C_f/C_{f_0} = R_f = 1 - DR$ and

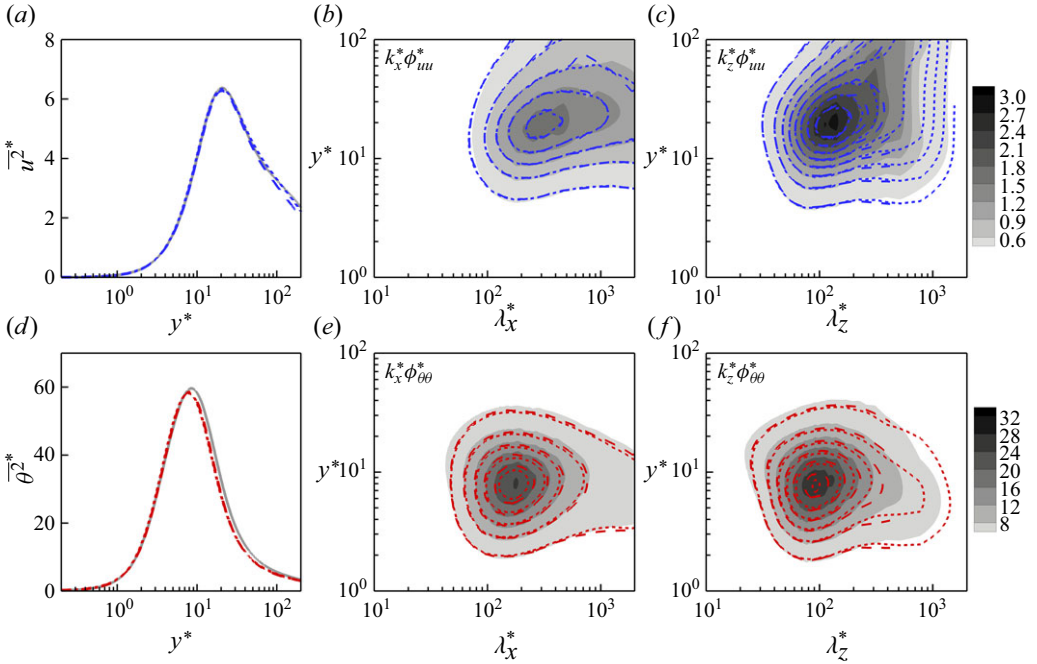


Figure 27. Comparison of (a) streamwise turbulent stress $\overline{u^2^*}$ and (d) mean square of turbulent temperature $\overline{\theta^2^*}$, as well as their pre-multiplied spectrograms $k_x^* \phi_{uu}^*$, $k_z^* \phi_{uu}^*$, $k_x^* \phi_{\theta\theta}^*$, $k_z^* \phi_{\theta\theta}^*$ (b,c,e,f) for the travelling wave at $Pr = 7.5$, $\omega^+ = 0.044$ (set 2, table 3). Solid grey line and grey-scale contour field: ‘full fine’ case. Dotted line and dotted contour lines: ‘full coarse’ case. Dashed line and dashed contour lines: ‘reduc. coarse’ case.

Case	κ_x^+	ω^+	L_x, L_z	Δ_x^+, Δ_z^+	Δ_y^+	C_{f_0}	C_{h_0}	DR %	HR %
Reduc. coarse	–	–	2.7h, 0.85h	8.3, 3.9	0.28 – 8.4	0.0057	5.47×10^{-4}	–	–
Reduc. inter.	–	–	2.7h, 0.85h	6.2, 2.6	0.18 – 5.6	0.0057	5.44×10^{-4}	–	–
Reduc. coarse	0.0014	0.088	7.6h, 0.85h	8.8, 3.9	0.28 – 8.4	–	–	29.5	43.5
Reduc. inter.	0.0014	0.088	7.6h, 0.85h	5.8, 2.6	0.18 – 5.6	–	–	28.6	43.1

Table 4. Validation cases at $Re_{\tau_0} = 590$ and $Pr = 20.0$.

$C_h/C_{h_0} = R_h = 1 - \text{HR}$, we can relate $\Delta \overline{U}_{log}^*$ and $\Delta \overline{\Theta}_{log}^*$ to R_f and R_h according to

$$\Delta \overline{U}_{log}^* = \sqrt{\frac{2}{C_{f_0}}} \left[\frac{1}{\sqrt{R_f}} - 1 \right] - \frac{1}{2\kappa_u} \ln R_f, \quad (C4a)$$

$$\Delta \overline{\Theta}_{log}^* = \frac{\sqrt{C_{f_0}/2}}{C_{h_0}} \left[\frac{\sqrt{R_f}}{R_h} - 1 \right] - \frac{1}{2\kappa_\theta} \ln R_f. \quad (C4b)$$

Equation (C4a) was first derived by Gatti & Quadrio (2016) (their equation 4.7). Equation (C4b) is new.

Appendix C. Statistics for the plane oscillation

See figures 28 and 29.

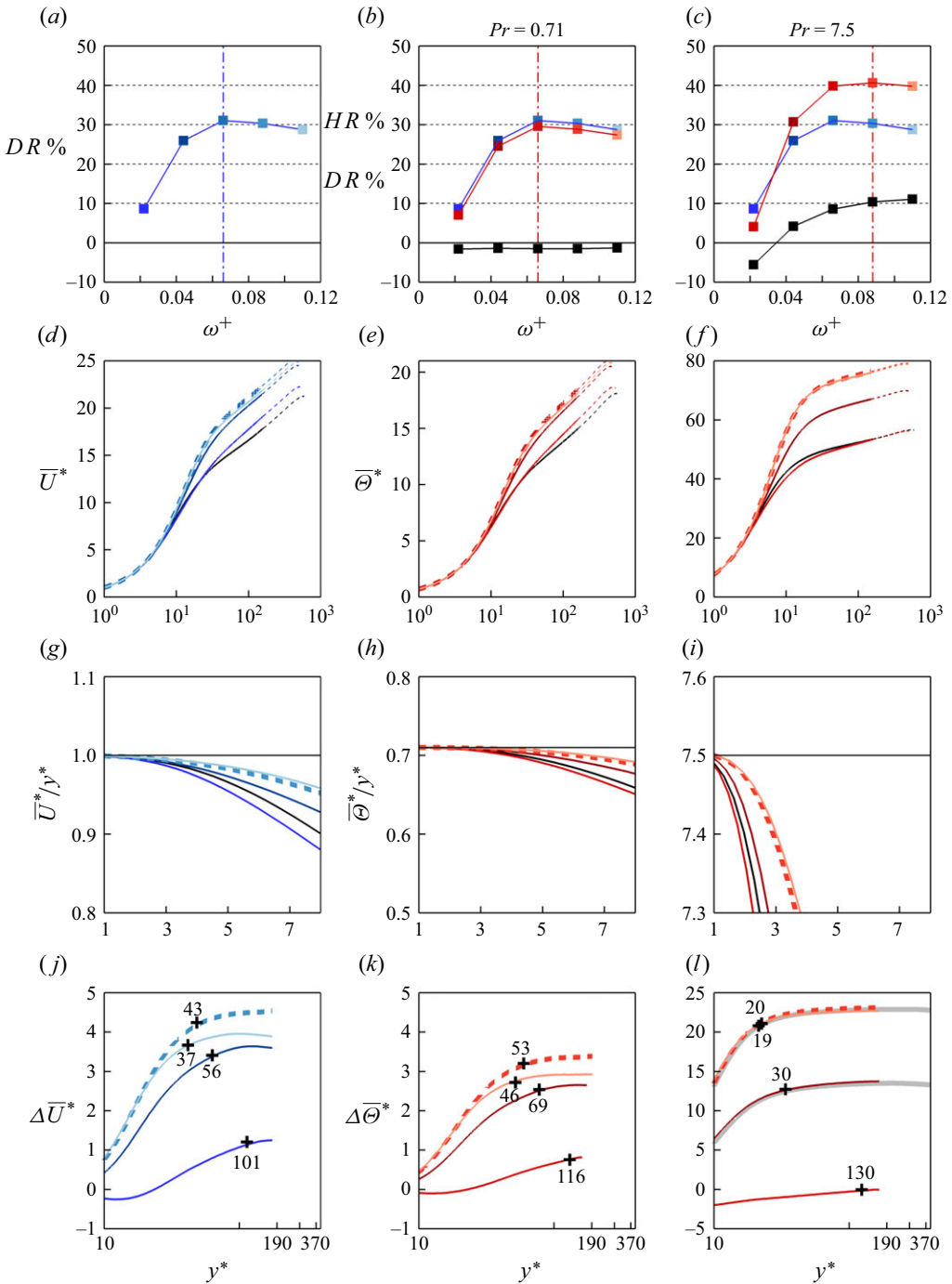


Figure 28. Same plots as in figure 8, but for the plane oscillation case with $A^+ = 12$.

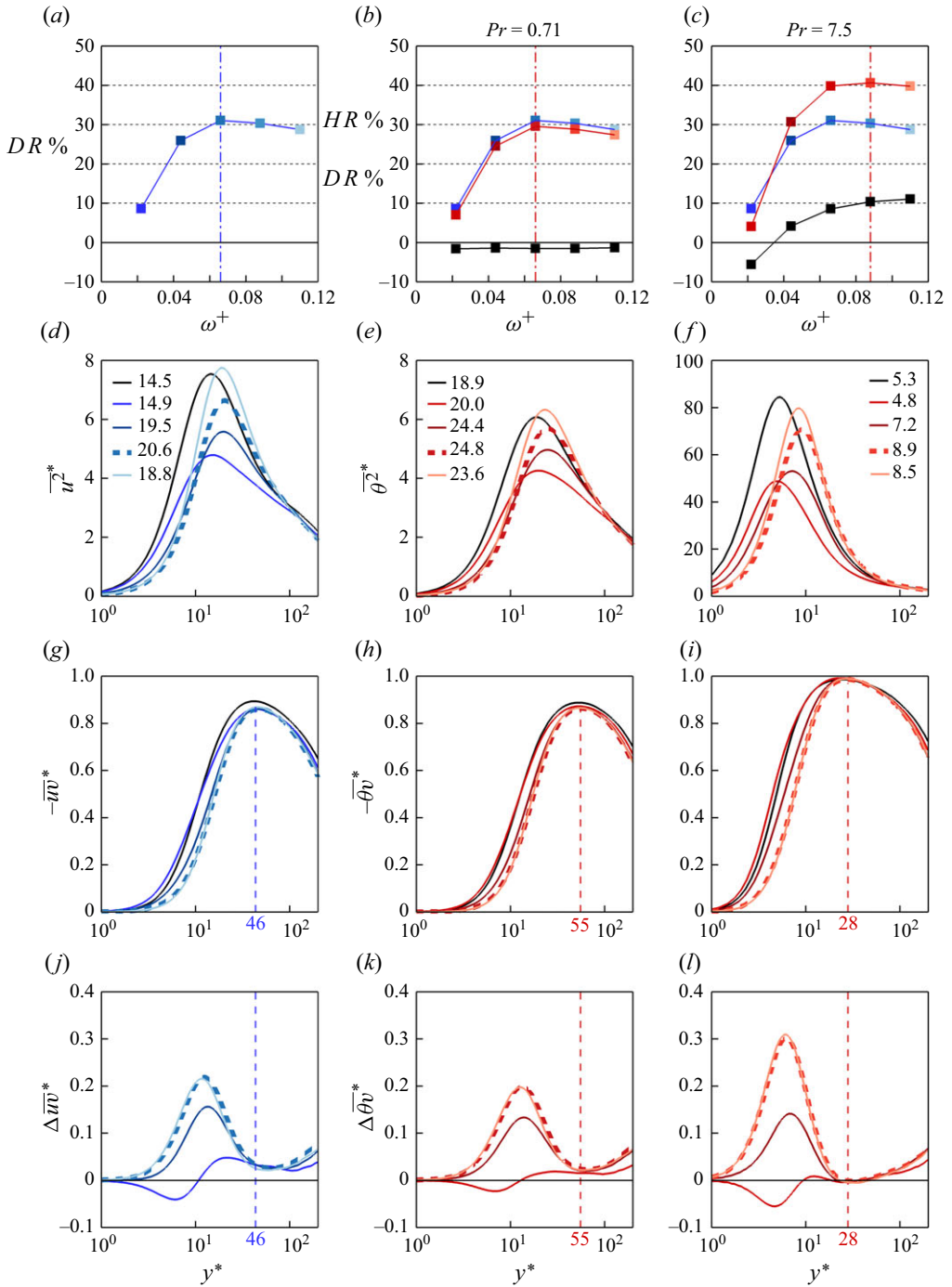


Figure 29. Same plots as in figure 9, but for the plane oscillation case with $A^+ = 12$.

- ALCÁNTARA-Á VILA, F. & HOYAS, S. 2021 Direct numerical simulation of thermal channel flow for medium–high Prandtl numbers up to $Re_\tau = 2000$. *Intl J. Heat Mass Transfer* **176**, 121412.
- ALCÁNTARA-Á VILA, F. & PÉREZ-QUILES, M.J. 2018 DNS of thermal channel flow up to $Re_\tau = 2000$ for medium to low Prandtl numbers. *Intl J. Heat Mass Transfer* **127**, 349–361.
- ALCÁNTARA-Á VILA, F. & PÉREZ-QUILES, M.J. 2021 Direct numerical simulation of thermal channel flow for $Re_\tau = 5000$ and $Pr = 0.71$. *J. Fluid Mech.* **916**, A29.
- BAEK, S., RYU, J., BANG, M. & HWANG, W. 2022 Flow non-uniformity and secondary flow characteristics within a serpentine cooling channel of a realistic gas turbine blade. *J. Turbomach.* **144** (9), 091002.
- BARON, A. & QUADRIO, M. 1995 Turbulent drag reduction by spanwise wall oscillations. *Appl. Sci. Res.* **55** (4), 311–326.
- BEWLEY, T.R., MOIN, P. & TEMAM, R. 2001 DNS-based predictive control of turbulence: an optimal benchmark for feedback algorithms. *J. Fluid Mech.* **447**, 179–225.
- BUNKER, R.S. 2013 Gas turbine cooling: moving from macro to micro cooling. In *ASME Turbo Expo*, pp. V03CT14A002. The American Society of Mechanical Engineers (ASME).
- CHANDRAN, D., ZAMPIRON, A., ROUHI, A., FU, M.K., WINE, D., HOLLOWAY, B., SMITS, A.J. & MARUSIC, I. 2023 Turbulent drag reduction by spanwise wall forcing. Part 2. High-Reynolds-number experiments. *J. Fluid Mech.* **968**, A7.
- CHILTON, T.H. & COLBURN, A.P. 1934 Mass transfer (absorption) coefficients prediction from data on heat transfer and fluid friction. *Ind. Engng Chem.* **26** (11), 1183–1187.
- CHOI, J.I., XU, C.X. & SUNG, H.J. 2002 Drag reduction by spanwise wall oscillation in wall-bounded turbulent flows. *AIAA J.* **40** (5), 842–850.
- CHOI, K.S. 2002 Near-wall structure of turbulent boundary layer with spanwise-wall oscillation. *Phys. Fluids* **14** (7), 2530–2542.
- CHOI, K.S. & CLAYTON, B.R. 2001 The mechanism of turbulent drag reduction with wall oscillation. *Intl J. Heat Fluid Flow* **22** (1), 1–9.
- CHOI, K.S., DEBISSCHOP, J.R. & CLAYTON, B.R. 1998 Turbulent boundary-layer control by means of spanwise-wall oscillation. *AIAA J.* **36** (7), 1157–1163.
- CHOI, K.S. & ORCHARD, D.M. 1997 Turbulence management using riblets for heat and momentum transfer. *Exp. Therm. Fluid Sci.* **15** (2), 109–124.
- CHUNG, D., CHAN, L., MACDONALD, M., HUTCHINS, N. & OOI, A. 2015 A fast direct numerical simulation method for characterising hydraulic roughness. *J. Fluid Mech.* **773**, 418–431.
- COLBURN, A.P. 1964 A method of correlating forced convection heat-transfer data and a comparison with fluid friction. *Intl J. Heat Mass Transfer* **7** (12), 1359–1384.
- DEAN, R.B. 1978 Reynolds number dependence of skin friction and other bulk flow variables in two-dimensional rectangular duct flow. *J. Fluids Engng* **100** (2), 215–223.
- DEL Á. LAMO, J.C. & JIMÉNEZ, J. 2009 Estimation of turbulent convection velocities and corrections to Taylor’s approximation. *J. Fluid Mech.* **640**, 5–26.
- DESHPANDE, R., CHANDRAN, D., SMITS, A.J. & MARUSIC, I. 2023 On the relationship between manipulated inter-scale phase and energy-efficient turbulent drag reduction. *J. Fluid Mech.* **972**, A12.
- DI CICCIA, G.M., IUSO, G., SPAZZINI, P.G. & ONORATO, M. 2002 Particle image velocimetry investigation of a turbulent boundary layer manipulated by spanwise wall oscillations. *J. Fluid Mech.* **467**, 41–56.
- DIPPREY, D.F. & SABERSKY, R.H. 1963 Heat and momentum transfer in smooth and rough tubes at various Prandtl numbers. *Intl J. Heat Mass Transfer* **6** (5), 329–353.
- ENDRIKAT, S., MODESTI, D., MACDONALD, M., GARCÍA-MAYORAL, R., HUTCHINS, N. & CHUNG, D. 2021 Direct numerical simulations of turbulent flow over various riblet shapes in minimal-span channels. *Flow Turbul. Combust.* **107** (1), 1–29.
- FAN, J.F., DING, W.K., ZHANG, J.F., HE, Y.L. & TAO, W.Q. 2009 A performance evaluation plot of enhanced heat transfer techniques oriented for energy-saving. *Intl J. Heat Mass Transfer* **52** (1–2), 33–44.
- FANG, J., LU, L. & SHAO, L. 2009 Large eddy simulation of compressible turbulent channel flow with spanwise wall oscillation. *Sci. China E: Phys. Mech. Astron.* **52** (8), 1233–1243.
- FANG, J., LU, L.P. & SHAO, L. 2010 Heat transport mechanisms of low Mach number turbulent channel flow with spanwise wall oscillation. *Acta Mechanica Sin.* **26** (3), 391–399.
- FOROOGHI, P., WEIDENLENER, A., MAGAGNATO, F., BÖHM, B., KUBACH, H., KOCH, T. & FROHNAPFEL, B. 2018 DNS of momentum and heat transfer over rough surfaces based on realistic combustion chamber deposit geometries. *Intl J. Heat Fluid Flow* **69**, 83–94.
- GATTI, D. & QUADRIO, M. 2013 Performance losses of drag-reducing spanwise forcing at moderate values of the Reynolds number. *Phys. Fluids* **25** (12), 125109.

- GATTI, D. & QUADRIO, M. 2016 Reynolds-number dependence of turbulent skin-friction drag reduction induced by spanwise forcing. *J. Fluid Mech.* **802**, 553–582.
- GATTI, D., QUADRIO, M., CHIARINI, A., GATTERE, F. & PIROZZOLI, S. 2024 Turbulent skin-friction drag reduction via spanwise forcing at high Reynolds number. E-print: ArXiv: 2409.07230, (physics, fluidyn).
- GUÉRIN, L., FLAGEUL, C., CORDIER, L., GRIEU, S. & AGOSTINI, L. 2024 Preferential enhancement of convective heat transfer over drag via near-wall turbulence manipulation using spanwise wall oscillations. *Intl J. Heat Fluid Flow* **110**, 109564.
- HAN, D., YU, B., WANG, Y., ZHAO, Y. & YU, G. 2015 Fast thermal simulation of a heated crude oil pipeline with a BFC-based POD reduced-order model. *Appl. Therm. Engng* **88**, 217–229.
- HASEGAWA, H., ISHITANI, H., MATSUHASHI, R. & YOSHIOKA, M. 1998 Analysis on waste-heat transportation systems with different heat-energy carriers. *Appl. Energy* **61** (1), 1–12.
- HASEGAWA, Y. & KASAGI, N. 2011 Dissimilar control of momentum and heat transfer in a fully developed turbulent channel flow. *J. Fluid Mech.* **683**, 57–93.
- HEALZER, J.M., MOFFAT, R.J. & KAYS, W.M. 1974 The turbulent boundary layer on a porous, rough plate: experimental heat transfer with uniform blowing. In *In Proc. Thermophys. Heat Transf. Conf.*, AIAA Paper 1974–680.
- HETSRONI, G., TISELI, I., BERGANT, R., MOSYAK, A. & POGREBNIYAK, E. 2004 Convection velocity of temperature fluctuations in a turbulent flume. *ASME J. Heat Transfer* **126** (5), 843–848.
- HUANG, Z., LI, Z.Y., YU, G.L. & TAO, W.Q. 2017 Numerical investigations on fully-developed mixed turbulent convection in dimpled parabolic trough receiver tubes. *Appl. Therm. Engng* **114**, 1287–1299.
- HURST, E., YANG, Q. & CHUNG, Y.M. 2014 The effect of Reynolds number on turbulent drag reduction by streamwise travelling waves. *J. Fluid Mech.* **759**, 11–55.
- IWAMOTO, K., FUKAGATA, K., KASAGI, N. & SUZUKI, Y. 2005 Friction drag reduction achievable by near-wall turbulence manipulation at high Reynolds numbers. *Phys. Fluids* **17** (1), 011702–011702.
- JIN, Y. & HERWIG, H. 2014 Turbulent flow and heat transfer in channels with shark skin surfaces: entropy generation and its physical significance. *Intl J. Heat Mass Transfer* **70**, 10–22.
- JUNG, W.J., MANGIAVACCHI, N. & AKHAVAN, R. 1992 Suppression of turbulence in wall-bounded flows by high-frequency spanwise oscillations. *Phys. Fluids* **4** (8), 1605–1607.
- KADER, B.A. 1981 Temperature and concentration profiles in fully turbulent boundary layers. *Intl J. Heat Mass Transfer* **24** (9), 1541–1544.
- KADER, B.A. & YAGLOM, A.M. 1972 Heat and mass transfer laws for fully turbulent wall flows. *Intl J. Heat Mass Transfer* **15** (12), 2329–2351.
- KAKAÇ, S., SHAH, R.K. & AUNG, W. 1987 *Handbook of Single-Phase Convective Heat Transfer*. Wiley.
- KANG, H.C. & KIM, M.H. 1999 Effect of strip location on the air-side pressure drop and heat transfer in strip fin-and-tube heat exchanger. *Intl J. Refrig.* **22** (4), 302–312.
- KARNIADAKIS, G.E. & CHOI, K.S. 2003 Mechanisms on transverse motions in turbulent wall flows. *Annu. Rev. Fluid Mech.* **35** (1), 45–62.
- KASAGI, N., TOMITA, Y. & KURODA, A. 1992 Direct numerical simulation of passive scalar field in a turbulent channel flow. *J. Heat Transfer* **114** (3), 598–606.
- KAYS, W.M., CRAWFORD, M.E. & WEIGAND, B. 1993 *Convective Heat and Mass Transfer*. McGraw-Hill.
- KIM, J. & HUSSAIN, F. 1993 Propagation velocity of perturbations in turbulent channel flow. *Phys. Fluids* **5** (3), 695–706.
- KUWATA, Y. 2021 Direct numerical simulation of turbulent heat transfer on the Reynolds analogy over irregular rough surfaces. *Intl J. Heat Fluid Flow* **92**, 108859.
- KUWATA, Y. 2022 Dissimilar turbulent heat transfer enhancement by Kelvin–Helmholtz rollers over high-aspect-ratio longitudinal ribs. *J. Fluid Mech.* **952**, A21.
- LEE, C., KIM, J. & CHOI, H. 1998 Suboptimal control of turbulent channel flow for drag reduction. *J. Fluid Mech.* **358**, 245–258.
- LI, W. & LI, G. 2010 Modeling cooling tower fouling in helical-rib tubes based on von Kármán analogy. *Intl J. Heat Mass Transfer* **53** (13–14), 2715–2721.
- LIU, C. & GAYME, D.F. 2020 An input–output based analysis of convective velocity in turbulent channels. *J. Fluid Mech.* **888**, A32.
- MA, Q., LUO, L., WANG, R.Z. & SAUCE, G. 2009 A review on transportation of heat energy over long distance: exploratory development. *Renew. Sustainable Energy Rev.* **13** (6–7), 1532–1540.
- MACDONALD, M., CHUNG, D., HUTCHINS, N., CHAN, L., OOI, A. & GARCÍA-MAYORAL, R. 2017 The minimal-span channel for rough-wall turbulent flows. *J. Fluid Mech.* **816**, 5–42.
- MACDONALD, M., HUTCHINS, N. & CHUNG, D. 2019 Roughness effects in turbulent forced convection. *J. Fluid Mech.* **861**, 138–162.

- MACDONALD, M., OOI, A., GARCÍA-MAYORAL, R., HUTCHINS, N. & CHUNG, D. 2018 Direct numerical simulation of high aspect ratio spanwise-aligned bars. *J. Fluid Mech.* **843**, 126–155.
- MARUSIC, I., CHANDRAN, D., ROUHI, A., FU, M.K., WINE, D., HOLLOWAY, B., CHUNG, D. & SMITS, A.J. 2021 An energy-efficient pathway to turbulent drag reduction. *Nat. Commun.* **12** (1), 1–8.
- MOSER, R.D., KIM, J. & MANSOUR, N.N. 1999 Direct numerical simulation of turbulent channel flow up to $Re_\tau = 590$. *Phys. Fluids* **11**, 943–945.
- NAGIB, H.M. & CHAUHAN, K.A. 2008 Variations of von Kármán coefficient in canonical flows. *Phys. Fluids* **20** (10), 101518.
- NG, C.S., OOI, A., LOHSE, D. & CHUNG, D. 2015 Vertical natural convection: application of the unifying theory of thermal convection. *J. Fluid Mech.* **764**, 349–361.
- OTTO, M., KAPAT, J., RICKLICK, M. & MHETRAS, S. 2022 Heat transfer in a rib turbulated pin fin array for trailing edge cooling. *J. Therm. Sci. Engng Appl.* **14**, 041012.
- PIROZZOLI, S. 2023 Prandtl number effects on passive scalars in turbulent pipe flow. *J. Fluid Mech.* **965**, A7.
- PIROZZOLI, S., BERNARDINI, M. & ORLANDI, P. 2016 Passive scalars in turbulent channel flow at high Reynolds number. *J. Fluid Mech.* **788**, 614–639.
- PIROZZOLI, S., ROMERO, J., FATICA, M., VERZICCO, R. & ORLANDI, P. 2022 DNS of passive scalars in turbulent pipe flow. *J. Fluid Mech.* **940**, A45.
- POPE, S.B. 2000 *Turbulent Flows*. Cambridge University Press.
- QUADRIO, M. 2011 Drag reduction in turbulent boundary layers by in-plane wall motion. *Phil. Trans. R. Soc. A* **369** (1940), 1428–1442.
- QUADRIO, M. & RICCO, P. 2011 The laminar generalized Stokes layer and turbulent drag reduction. *J. Fluid Mech.* **667**, 135–157.
- QUADRIO, M., RICCO, P. & VIOTTI, C. 2009 Streamwise-travelling waves of spanwise wall velocity for turbulent drag reduction. *J. Fluid Mech.* **627**, 161–178.
- QUADRIO, M. & STIBILLA, S. 2000 Numerical simulation of turbulent flow in a pipe oscillating around its axis. *J. Fluid Mech.* **424**, 217–241.
- RANI, P. & TRIPATHY, P.P. 2022 Experimental investigation on heat transfer performance of solar collector with baffles and semicircular loops fins under varied air mass flow rates. *Intl J. Therm. Sci.* **178**, 107597.
- RICCO, P. 2004 Modification of near-wall turbulence due to spanwise wall oscillations. *J. Turbul.* **5**, 024.
- RICCO, P., OTTONELLI, C., HASEGAWA, Y. & QUADRIO, M. 2012 Changes in turbulent dissipation in a channel flow with oscillating walls. *J. Fluid Mech.* **700**, 77–104.
- RICCO, P., SKOTE, M. & LESCHZINER, M.A. 2021 A review of turbulent skin-friction drag reduction by near-wall transverse forcing. *Prog. Aerosp. Sci.* **123**, 100713.
- RICCO, P. & WU, S. 2004 On the effects of lateral wall oscillations on a turbulent boundary layer. *Exp. Therm. Fluid Sci.* **29** (1), 41–52.
- ROUHI, A., CHUNG, D. & HUTCHINS, N. 2019 Direct numerical simulation of open-channel flow over smooth-to-rough and rough-to-smooth step changes. *J. Fluid Mech.* **866**, 450–486.
- ROUHI, A., ENDRIKAT, S., MODESTI, D., SANDBERG, R.D., ODA, T., TANIMOTO, K., HUTCHINS, N. & CHUNG, D. 2022 Riblet-generated flow mechanisms that lead to local breaking of Reynolds analogy. *J. Fluid Mech.* **951**, A45.
- ROUHI, A., FU, M.K., CHANDRAN, D., ZAMPIRON, A., SMITS, A.J. & MARUSIC, I. 2023 Turbulent drag reduction by spanwise wall forcing. Part 1: large-eddy simulations. *J. Fluid Mech.* **968**, A6.
- ROUHI, A., LOHSE, D., MARUSIC, I., SUN, C. & CHUNG, D. 2021 Coriolis effect on centrifugal buoyancy-driven convection in a thin cylindrical shell. *J. Fluid Mech.* **910**, A32.
- ROWIN, W.A., ZHONG, K., SAURAV, T., JELLY, T., HUTCHINS, N. & CHUNG, D. 2024 Modelling the effect of roughness density on turbulent forced convection. *J. Fluid Mech.* **979**, A22.
- SCHLÜNDER, E.U. 1998 Analogy between heat and momentum transfer. *Chem. Engng Process. Process Intensif.* **37** (1), 103–107.
- SCHWERTFIRM, F. & MANHART, M. 2007 DNS of passive scalar transport in turbulent channel flow at high Schmidt numbers. *Intl J. Heat Fluid Flow* **28** (6), 1204–1214.
- SHAW, D.A. & HANRATTY, T.J. 1977 Turbulent mass transfer rates to a wall for large Schmidt numbers. *AIChE J.* **23** (1), 28–37.
- STALIO, E. & NOBILE, E. 2003 Direct numerical simulation of heat transfer over riblets. *Intl J. Heat Fluid Flow* **24** (3), 356–371.
- TOUBER, E. & LESCHZINER, M.A. 2012 Near-wall streak modification by spanwise oscillatory wall motion and drag-reduction mechanisms. *J. Fluid Mech.* **693**, 150–200.
- UMAIR, M., TARDU, S. & DOCHE, O. 2022 Reynolds stresses transport in a turbulent channel flow subjected to streamwise traveling waves. *Phys. Rev. Fluids* **7** (5), 054601.

- VENGADESAN, E. & SENTHIL, R. 2020 A review on recent developments in thermal performance enhancement methods of flat plate solar air collector. *Renew. Sustainable Energy Rev.* **134**, 110315.
- VIOTTI, C., QUADRIO, M. & LUCHINI, P. 2009 Streamwise oscillation of spanwise velocity at the wall of a channel for turbulent drag reduction. *Phys. Fluids* **21** (11), 115109.
- WALSH, M.J. & WEINSTEIN, L.M. 1979 Drag and heat-transfer characteristics of small longitudinally ribbed surfaces. *AIAA J.* **17** (7), 770–771.
- WATANABE, K. & TAKAHASHI, T. 2002 LES simulation and experimental measurement of fully developed ribbed channel flow and heat transfer. In *ASME Turbo Expo*, vol. **36088**, pp. 411–417. The American Society of Mechanical Engineers (ASME).
- XIE, X. & JIANG, Y. 2017 Absorption heat exchangers for long-distance heat transportation. *Energy* **141**, 2242–2250.
- YAMAMOTO, A., HASEGAWA, Y. & KASAGI, N. 2013 Optimal control of dissimilar heat and momentum transfer in a fully developed turbulent channel flow. *J. Fluid Mech.* **733**, 189–220.
- YAO, J., CHEN, X. & HUSSAIN, F. 2022 Direct numerical simulation of turbulent open channel flows at moderately high Reynolds numbers. *J. Fluid Mech.* **953**, A19.
- YU, B., LI, C., ZHANG, Z., LIU, X., ZHANG, J., WEI, J., SUN, S. & HUANG, J. 2010 Numerical simulation of a buried hot crude oil pipeline under normal operation. *Appl. Therm. Engng* **30** (17–18), 2670–2679.
- YUAN, J. & PIOMELLI, U. 2014 Estimation and prediction of the roughness function on realistic surfaces. *J. Turbul.* **15** (6), 350–365.
- YUAN, Q., LUO, Y., SHI, T., GAO, Y., WEI, J., YU, B. & CHEN, Y. 2023 Investigation into the heat transfer models for the hot crude oil transportation in a long-buried pipeline. *Energy Sci. Engng* **11** (6), 2169–2184.
- ZHONG, K., HUTCHINS, N. & CHUNG, D. 2023 Heat-transfer scaling at moderate Prandtl numbers in the fully rough regime. *J. Fluid Mech.* **959**, A8.